Design of Anisotropically-Shaped Plasmonic Nanocrystals from Ultrasmall Sn-Decorated In_2O_3 Nanoclusters Used as Seed Materials

Gregory A Davis Jr.,[1,#] Gyanaranjan Prusty,[1,#] Sumon Hati,[1] Jacob T. Lee,[1] Sarah R. Langlais,[1] Xun Zhan,[2] and Rajesh Sardar*[,1]

[1]Department of Chemistry and Chemical biology, Indiana University-Purdue University Indianapolis, Indianapolis, Indiana 46202, United States

[2]Department of Chemistry, Indiana University, Bloomington, Indiana 47405, United States

#These authors contributed equally to this work.

*Corresponding author email: rsardar@iupui.edu

This is the author's manuscript of the article published in final edited form as:

Davis, G. A. Jr., Prusty, G., Hati, S., Lee, J. T., Langlais, S. R., Zhan, X., & Sardar, R. (2022). Design of Anisotropically Shaped Plasmonic Nanocrystals from Ultrasmall Sn-Decorated In2O3 Nanoclusters Used as Seed Materials. The Journal of Physical Chemistry C, 126(50), 21438–21452. https://doi.org/10.1021/acs.jpcc.2c06572

Abstract

Ultrasmall inorganic nanoclusters (<2.0 nm in diameter) bridge the gap between individual molecules and large nanocrystals (NCs) and provide the critical foundation to design and prepare new solid-state nanomaterials with previously unknown properties and functions. Herein, for the first time, we report a monodispersed colloidal synthesis, and successful isolation of metastable rhombohedral phase <2.0 nm indium oxide (In_2O_3) nanoclusters. Ultrasmall nanocluster formation is controlled by the kinetically driven growth process, as evaluated through the variation of metal-to-passivating ligand concentrations. Although, <2.0 diameter In_2O_3 nanoclusters are synthesized in the presence of tin (Sn)-precursor, they do not display typical localized surface plasmon resonance (LSPR) properties, which are commonly observed in Sn-doped In_2O_3 (Sn:In_2O_3) NCs. Our Raman and X-ray photoelectron spectroscopy, and high-resolution transmission electron (HRTEM) analyses support the existence of Sn-decorated In_2O_3 nanoclusters where Sn-complexes reside on the surface of the nanocluster as Z-type ligands as opposed to the formation of Sn:In_2O_3 nanoclusters, which behave wide band-gap (~5.5 eV) nanomaterials. The experimentally determined band-gap is good agreement with the theoretical effective mas calculations. Newly synthesized Sn-decorated, 1.7 nm diameter In_2O_3 nanoclusters are further used as reactive monomers for the seeded growth synthesis of *bcc*-phase, plasmonic Sn:In_2O_3 NCs via *ex situ* injection of In-precursors without addition of any Sn-precursors. The LSPR peak of Sn:In_2O_3 NCs, which appear to form nanoflower assemblies, is tunable between 1800-4000 nm region and possibly even the deep IR region. In addition to altering the size and assembly of spherical Sn:In_2O_3 NCs by introducing different amounts of indium acetylacetonate, injection of indium chloride precursors in the reaction mixture results in the formation of rod-shaped NCs. Surprisingly, Sn-decorated, <1.5 nm diameter In_2O_3 nanoclusters do not grow to large plasmonic Sn:In_2O_3 NCs. Taken together, the results presented here contribute to the fundamental understanding of the surface free energy of ultrasmall metal oxide nanoclusters and further advance the knowledge of phase transformation and growth of plasmonic NCs.

Introduction

Ultrasmall inorganic nanoclusters with sizes between 1-3 nm display unique optoelectronic (absorption and photoluminescence) and magnetic properties that are different from large-sized nanocrystals (NCs).[1-2] Interestingly, ultrasmall noble metal (Ag and Au) nanoclusters exhibit “molecule-like” multiple electronic states with distinct electronic transitions observed in absorption spectroscopy. Semiconductor metal chalcogenide (e.g., CdSe and CdS) nanoclusters with <2.0 nm in diameter display extremely sharp excitonic peaks and broad emission features covering the entire visible region.[3-4] Furthermore, as the size of the nanoclusters reach <2.0 nm, nearly 80% of the atoms are present on the surface.[5] Therefore, the surface structure strongly governs the physical, chemical, and optoelectronic properties. In particular, Robinson and coworkers reported chemical-induced isomerization of ultrasmall cadmium chalcogenide nanoclusters, which displayed distinct excitonic peak position depending on the isomeric forms.[6] Our group, and others, showed that modification of the surface of ultrasmall metal chalcogenide nanoclusters with appropriate ligands dramatically changes the absorption and photoluminescence properties because of the delocalization of excitonic wave functions at the nanocluster-ligand interface.[7-8] Finally, it has been shown that ultrasmall noble metal[9] and metal chalcogenide[10] nanoclusters can serve as active precursors for the synthesis of anisotropically-shaped NCs. Together, ultrasmall inorganic nanoclusters display multi-faceted roles in fundamental chemical processes, thus it is a paramount importance to synthesize, isolate, and characterize nanoclusters composed of new inorganic components to further advance the field.

Over the last three decades, extensive work has been done to synthesize ultrasmall noble metal[1, 11] and metal chalcogenide[12-14] nanoclusters. In this context, only a handful of synthetic methods have been developed to prepare ultrasmall, metal-oxide nanoclusters.[15] The property of metal oxide nanoclusters and/or NCs can be tuned by controlled manipulation of inorganic core composition, crystallographic structure, morphology, and surface stoichiometry. Metal oxide NCs are more stable at elevated temperature and physiological media than either noble metal or metal chalcogenide NCs, allowing them to find applications in gas sensing,[16] media information processing

and storage,[17] bioimaging and biosensing,[18] etc. Another unique structural property of metal-oxide NCs is their ability to allow substitution of lattice atoms by aliovalent ("extrinsic") dopants to synthesize Sn-doped In_2O_3 ($Sn:In_2O_3$), Al-/In-/F-doped ZnO, and In-doped CdO NCs.[19-22] Doped semiconductor metal oxides can induce electrons to occupy conduction band positions through increased overlap of early d-orbital transition series. The introduction of substituent atoms into the crystal lattice is highly attractive because their valence band electrons can be transferred into the conduction band of host crystals.[23-24] Conduction band electrons can then act as free charge carriers and collectively oscillate upon exposure to incident light that generates localized surface plasmon resonance (LSPR) properties.[25] The unique advantage of metal-oxide NC-based LSPR property is that the plasmon resonance can be tuned in the near (NIR)-to-mid infrared region of the solar spectrum, as opposed to only the visible region LSPR signature by Ag and Au NCs. Therefore, doped metal-oxide NCs have been used for various potential applications that require light-matter interactions in the entire infrared region.[26] Furthermore, free electron density (N_e) directly affects the electronic and optical properties of metal-oxide NCs.[27] Therefore, there is fine balance between making metal-oxide NCs highly conductive (increasing the N_e value) while keeping the LSPR wavelength in the NIR region (reducing the N_e value) for transparency in the visible region.

Amongst many metal oxides, $Sn:In_2O_3$, which is an n-type transparent conducting oxide, has been extensively researched due to many potential applications starting from gas sensing devices,[28] solar cells,[29] and flat panel display technology and other solid-state devices.[30] Since the first reproducible colloidal synthetic method reported by Kanehara et al.[20] on LSPR active $Sn:In_2O_3$ NCs, many studies have been conducted to delineate the fundamental structure-property relationship.[31-32] The LSPR wavelength of $Sn:In_2O_3$ NCs can be tuned over the entire infrared region by systematically controlling either In/Sn ratio in a particular size or varying the size of the NCs.[33] Although, extensive LSPR-based studies have been conducted with larger $Sn:In_2O_3$ NCs (>3.0 nm diameter), it is still unknown whether ultrasmall $Sn:In_2O_3$ nanoclusters could support extrinsic doping and LSPR properties. Furthermore, it would be important to examine if ultrasmall $Sn:In_2O_3$ nanoclusters retain their reactivity for use as precursors in

synthesizing anisotropically-shaped NCs, as demonstrated for noble metal and metal chalcogenides systems.[2, 34-36]

In this article, we report the first colloidal synthesis and isolation of metastable, rhombohedral (rh) phase, ultrasmall (<2.0 nm diameter) In_2O_3 nanoclusters. To our surprise, extensive structural characterizations by spectroscopy and microscopy techniques suggest that Sn dopants preferentially reside on the surface of In_2O_3 nanoclusters and do not incorporate within the inorganic lattice. The X-ray photoelectron spectroscopy (XPS) analysis supports In-Sn interactions. The formation of Sn-decorated In_2O_3 nanoclusters is a kinetically controlled method where concentration of surface passivating ligands dictates the final nanocluster diameter, dispersity, and optoelectronic properties. Ultrasmall nanoclusters do not show LSPR properties, instead displaying the typical n-type band gap, which follows the quantum confinement effect.[37] Most importantly, utilizing non-LSPR Sn-decorated In_2O_3 nanoclusters as seeds, LSPR active Sn:In_2O_3 spherical NCs and nanorods (NRs) are synthesized just by introducing new In-precursors without the addition of Sn-precursors, suggesting that the surface of ultrasmall NC retain their reactivity. We determine that the anionic counterpart of the In-precursor dictates the final shape of Sn:In_2O_3 NCs. Our time-dependent microscopy analysis supports the continuous growth mechanism where the availability of In-precursor dictates the growth process, thus NC size is not limited. We demonstrate the control over LSPR wavelengths of Sn:In_2O_3 NCs by tuning the peak position from ~1800 to ~4000 nm, thus effectively manipulating their N_e values as a function of size. Taken together, the colloidal approach we demonstrate here shows the importance of ultrasmall nanoclusters in the field of chemistry and nanotechnology that could open new methods of synthesizing previously unknown metal-oxide NCs with tunable optoelectronic properties.

Experimental Section

Materials. Indium acetylacetonate ($In(acacc)_3$, ≥99.99%), tin (IV) acetate ($Sn(acetate)_4$, 99%), myristic acid (MA, ≥99%), indium chloride ($InCl_3$), *N*,*N*,*N*′,*N*′-tetramethylethane-1,2-diamine (98%) (TMEDA), oleic acid (OLAc, 99%), 1-octadecene (ODE, 90%), oleylamine (OLAm,70%), were purchased from Sigma-Aldrich. All chemicals were used without further purification. Solvents (toluene, chloroform, and ethanol) were purchased from Fisher scientific and purged with N_2 for at least 30 min prior to use.

Synthesis and purification of ultrasmall Sn-decorated In_2O_3 nanoclusters. Ultrasmall Sn-decorated In_2O_3 nanoclusters were synthesized via modification of a literature procedure[38] as follows: 0.206 g (0.5 mmol) of $In(acac)_3$, 0.0345 g (0.10 mmol) $Sn(acetate)_4$, and 1.026-0.912 g (4.5-4.0 mmol) MA were mixed in 10 mL of 1-ODE and in a three-neck 50 mL round bottom connected to a Schlenk line. This reaction mixture was purged with N_2 at 110° C for 30 min. Then the temperature was increased to 130° C and flask was kept under vacuum for 1 h and 45 min and then returned to N_2. The temperature of the reaction increased to 290° C and at this point a separately prepared N_2 purged solution of 0.98 mL of OLAm in 1 mL of ODE was injected quickly through a syringe. Addition of the OLA-ODE mixture cooled the temperature to 270° C. The reaction mixture was stirred at this temperature for 1h. Finally, the temperature was reduced further to 230˚ C and stirred for another 1h under N_2. Approximately 10 mL chloroform was added to quench the reaction. Then, the total 20 mL reaction solution was separated into two 50 mL centrifuge tubes having 10 mL each. Next, 35 mL of warm ethanol (~50° C) was added in each of the tube and centrifuged at 10,000 rpm for 10 min to precipitate nanoclusters. The second step of purification involved addition of 5 mL of chloroform, followed by sonication for at least 5 min to complete dispersed nanoclusters. 20 mL of warm ethanol was added in both tubes and centrifuged at 10,000 rpm for 10 min. This purification step was repeated for an additional time. Next, purified nanoclusters were dissolved in 2 mL of chloroform and transferred to a 20 mL glass vial and the solvent was dried by a rotary evaporator. Finally, nanocluster solid was stored under N2 for further characterizations.

Seeded growth synthesis of Sn:In_2O_3 NCs. 30 mg of purified ultrasmall Sn-decorated In_2O_3 nanoclusters were dispersed in 2.5 mL of ODE and sonicated for 15 min and transferred to a three-neck round bottom flask. In the same ODE solution, 30 mg of $In(acac)_3$ and 30 mg of MA were added. The reaction mixture was purged under N_2 at 110° C for 30 min. Then the temperature was increased to 130˚ C and flask was kept under high vacuum for 15 min and the returned to N_2. The temperature of the flask was increased to 290 ˚C. At this junction, a mixture of 0.3 mL of OLAm and 0.3 mL of ODE was quickly injected through. The temperature of the reaction mixture then adjusted to 270° C and stirred for 5h. The reaction was quenched by addition of 3 mL chloroform, and Sn:In_2O_3 NCs were purified using the ethanol-induced precipitation approach as mentioned above.

Seeded growth synthesis of Sn:In_2O_3 nanorods. In a 3-neck, 50 mL round bottom flask, 50 mg of ultrasmall Sn-decorated In_2O_3 nanoclusters, 0.18 mmol $InCl_3$, 2.21 mmol (~0.7mL) OLAc, 5.00 mL ODE, and 2.2 mL OLAm mixture together. The reaction mixture then stirred under vacuum at room temperature for 30 min, and then transferred to at N_2 and stirred for another 1h. Next, it was heated to 290° C for 4 hr, and after that solution was allowed to cool to room temperature. Sn:In_2O_3 nanorods were purified first by dissolving in 5 mL chloroform and then precipitated out by adding 30 mL warm isopropanol. Nanorods were isolated via centrifugation at 5000 rpm for 5 min. The purification process was repeated for another time and then Sn:In_2O_3 nanorods were dispersed in 5 mL toluene and stored in a glove box.

Synthesis of plasmonic Sn:In_2O_3 NCs. We used a literature procedure to synthesize plasmonic, 5.5 nm Sn:In_2O_3 NCs.[38] Briefly, 0.412 g (1.0 mmol) $In(acac)_3$, 0.071 g (0.2 mmol) $Sn(acetate)_4$, and 0.685 g (3.0 mmol) MA were mixed in 20 mL ODE and the reaction mixture was degassed at 110° C for 1h and then heated to 295 ^{O}C under N_2. Once the temperature stabilized, 3 mL of OLAm in ODE was injected that resulted in a drop of reaction temperature to 270° C, which was maintained for 4h for the growth of Sn:In_2O_3 NCs. NCs were the purified

using the solvent induced precipitation method as described in "Seeded growth synthesis of Sn:In_2O_3 NCs."

TMEDA replacement reaction. 60 mg of purified, ultrasmall In_2O_3 nanoclusters was dissolved in 10 mL chloroform to prepare a homogeneous solution. Then 0.30 mL (of TMEDA was added while stirring under N_2 atmosphere for 24h at room temperature. Initially, 2, 4, 8, 12, and 24hr a 2 mL aliquot was removed, nanoclusters were purified using solvent-assisted precipitation and then EDS analysis was conducted.

Microscopy and Spectroscopy Characterizations.

XRD analysis: A Bruker D8 Discover X-ray diffractometer (Cu Kα, λ = 1.54 Å) was used to collect XRD patterns. Chloroform dispersion of purified nanoclusters/NCs was drop-cast onto cleaned glass coverslips. A 2D VÅNTEC-500 detector was used to obtain diffraction patterns from 10-60° 2θ with 5° 2θ steps and 30 s per step. Combined diffraction patterns were integrated to create 1D output.

SEM-EDS analysis: Elemental analysis was conducted on a field emission scanning electron microscopy system (Hitachi S-4700), which was equipped with an energy dispersive X-ray (EDS) analyzer.

TEM analysis: TEM analysis was conducted using a JEOL-JEM-F200 electron microscope with an accelerating voltage of 200 kV. TEM samples were prepared by dispersing in $CHCl_3$ and dropping 10 µL onto a carbon-coated 150 mesh copper grid (Electron Microscopy Science). The excess solution was drawn through with a filter paper.

UV-Vis-NIR and photoluminescence emission measurements. The absorption spectra were collected using a Perkin Elmer Lambda 19 UV/Visible/NIR spectrometer in a 1.0 cm quartz cuvette over a range of 300-3000 nm. The cuvette was cleaned with aqua regia to remove any adsorbed organics. Samples were dispersed in carbon tetrachloride (CCl_4). The photoluminescence emission spectra were collected using a Cary Eclipse fluorescence spectrophotometer from Varian Instruments with 1 cm quartz cuvettes at 360 nm excitation wavelength.

XPS analysis: XPS was conducted at the Chapel Hill Analytical and Nanofabrication Laboratory. Samples were prepared by drop-casting purified samples onto piranha-cleaned silicon wafers. A Kratos Axis Ultra DLD X-ray photoelectron spectrometer with Al Kα X-ray irradiation and energies of 80 and 20 eV were used for a survey and high-resolution scans, respectively. For samples that were electrically conductive, the sample was grounded, and the charge neutralizer was turned off. If samples showed some slight differential charging, then in these cases, the charge neutralizer was used, but the sample was isolated from ground. All spectra were corrected to the C 1s peak at 284.6 eV.

FTIR analysis: A Thermo Scientific Nicolet iS10 spectrometer with accompanying Omnic 8.2 software was used for all FTIR collection and processing. FTIR ligand study was performed using a KBr pellet which was a mixture of ~10mg of ultrasmall nanoclusters in ~70mg of KBr salt and finely ground and mixed using a mortar and pestle. The mixture was then pressed into a pellet using a KBr pellet press with adapters. The sample was held in place by a plate holder accessory and scanned for 200 scans with a background of a KBr only pellet for 64 scans from 400 – 4000 cm^{-1}. For the LSPR study of 11.4 nm NCs, a Pike Industries FTIR liquid cell was used. A solution of ~60 mg of NCs was dispersed into 2 mL of CCl_4 and injected into the liquid cell. The cell was then placed in the holder and scanned for 100 scans with a background of CCl_4 64 scans from 400 – 7800 cm^{-1}.

Raman spectroscopy: Samples were drop casted on cleaned silicon wafers and spectra were acquired using a XploRA Plus Raman Microscope from Horiba Scientific. Crystal lattice vibration related spectra were obtained using a 532 nm laser at 25% power, 1800 line/mm grating and 10x objective were used to collect spectra with an acquisition time of 3 second and

3 to 5 accumulations. Spectra delineating the vibrational modes of ligands were obtained using 532 nm laser at 1% power with a 100x objective and 60 second acquisition times over 3 accumulations.

TDDFT calculations: Theoretical calculations were performed to obtain frequenquency optimized geometry and determine Raman vibrational frequencies for different modes of Sn-alkylcarboxylate bonded to the O atom via Sn-O bonds. Calculations were accomplished using Gaussian16[39] with the BP86 exchange-correlation functional in the GenECP variation. LanL2DZ effective core potential basis set[40] was used for In, O and Sn atom while 6-311+G** basis set was used for rest of the atoms to perform the theoritical calculation.

Results and Discussion

Synthesis and Characterization of Ultrasmall, Sn-Decorated In_2O_3 Nanoclusters:

In the traditional high-temperature colloidal approach, the key to producing nearly monodisperse inorganic nanoclusters is to balance the reactivity between the metal precursors using passivating ligands and reaction temperature.[11, 41] Herein, we have adapted a high temperature colloidal synthetic route to prepare Sn-decorated In_2O_3 nanoclusters with a detailed procedure provided in the Experimental section. As schematically shown in **Figure 1A**, in a standardized approach, 0.5 mmol of indium

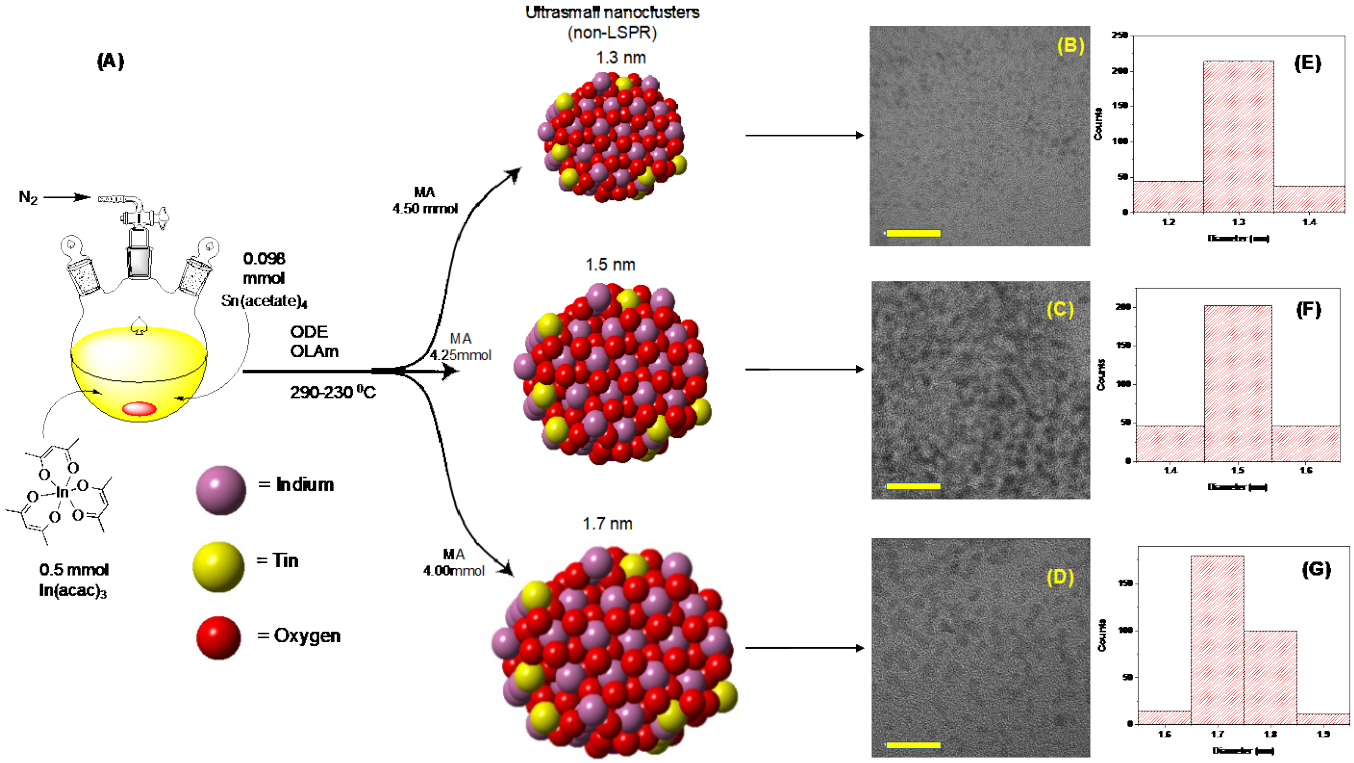

Figure 1. *(A) Schematic representation for the synthesis of ultrasmall Sn-decorated In_2O_3 nanoclusters. For simplicity, no surface passivating ligands are displayed. (B)-(D) HRTEM images 1.3, 1.5, and 1.7 nm diameter, of tin decorated Sn-decorated ultrasmall In_2O_3 nanoclusters. Scale bars are 20 nm. (E)-(F) Corresponding histograms of size analysis, determined using ImageJ software counting >300 particles.*

acetylacetonate [$In(acac)_3$] and 0.098 mmol of tin acetate [$Sn(acetate)_4$] were mixed in 10 mL 1-octadecene along with various molar amounts of myristic acid (MA, 4.0-4.5 mmol). The reaction mixture underwent multiple cycles of vacuum and nitrogen (N_2) and then heated to 290 °C under N_2. At this temperature ~2.0 mL, 1-ODE solution of oleylamine (OLAm) was injected and then reduced the reaction temperature to 270 °C for 1 hr, finally an additional 1 hr aging at 230 °C resulted in a faint yellow colored solution. The nanoclusters obtained were purified using a solvent-induced precipitation method and characterized to determine their structural and photophysical properties.

Transmission electron microscopy (TEM) analysis of the purified product showed the presence of highly monodisperse ultrasmall nanoclusters that appeared to be spherical in shape (**Figure 1B-G**). Depending on the MA:In^{3+} mole ratio of 9.0, 8.5, and 8.0, the size of nanoclusters is controlled to be 1.3, 1.5, and 1.7 nm, respectively.

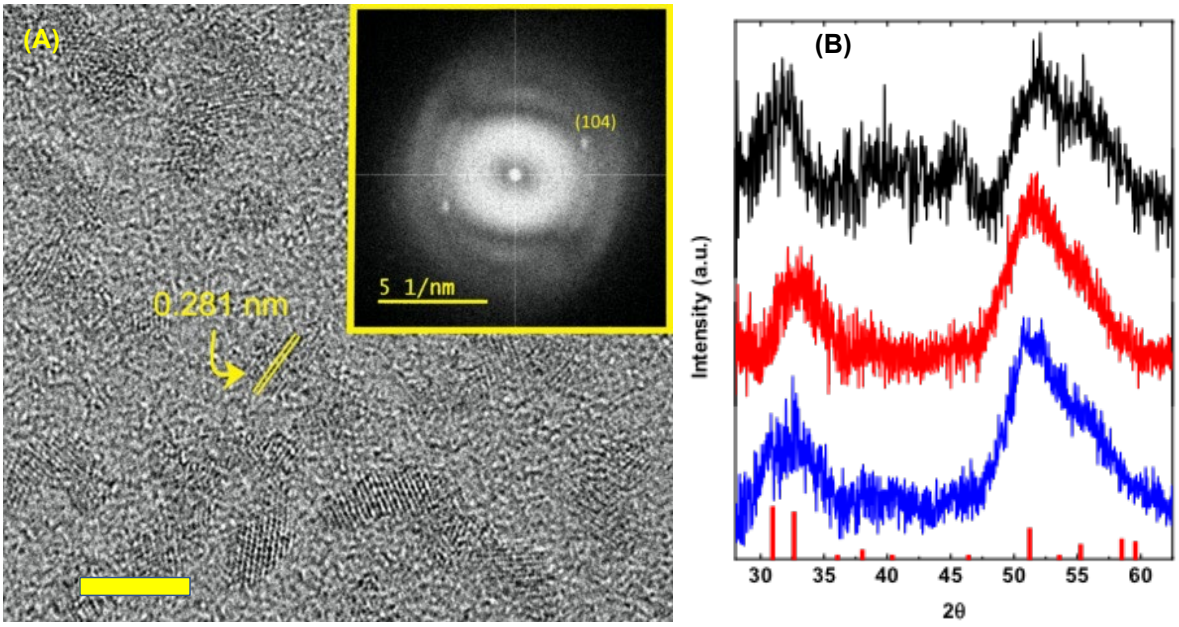

Figure 2. *(A) HRTEM image and SAED diffraction of 1.7 nm, Sn-decorated In_2O_3 nanoclusters. The value of 0.281 nm represents spacing between the (104) plane of rh-In_2O_3. The scale bar is*

2 nm. (B) XRD patterns of Sn-decorated In_2O_3 nanoclusters with all three different sizes. The rhombohedral (rh) In_2O_3 standard is shown at the bottom of panel B (JCPDS 21-0406).

The experimental parameters, size and properties of nanoclusters are summarized in Table S1. The high-resolution TEM (HRTEM) image shown in **Figure 2A** for 1.7 nm nanoclusters indicates that they are well formed single crystals with the inter-planar distance of 0.281 nm for the (104) plane. This lattice spacing is consistent with rh-phase In_2O_3.[42] Although corundum-type, rh-In_2O_3 is a metastable phase that belongs to the hexagonal crystal family and can be synthesized at elevated temperature (>800 ° C).[43] Radovanovic and coworkers reported the first colloidal synthesis of rh-In_2O_3 NCs with >3.0 nm in diameter,[44] however, to the best of our knowledge, we report the first example where <2.0 nm nanoclusters that are synthesized and isolated using a colloidal method. Importantly, we believe that the presence of a large excess of anionic ligands (M) stabilizes the hexagonal unit cell. We elected to perform analysis on the 1.7 nm nanoclusters for HRTEM and selected area diffraction analysis because performing analyses are challenging for nanoclusters smaller than <1.5 nm. Nevertheless, as shown in **Figure 2B**, powder X-ray diffraction (XRD) patterns were recorded of all three sizes of nanoclusters. The XRD patterns are in good agreement with corundum-type rh-In_2O_3, specifically the appearance of (104) and (116) planes 2θ of ~31˚ and 52°, respectively (JCPDS 21-0406).[44] The broad XRD pattern is very common for ultrasmall inorganic nanoclusters.[45]

Examination of the Photophysical Properties of Ultrasmall, Sn-Decorated In_2O_3 Nanoclusters: As described above, our ultrasmall In_2O_3 nanoclusters were synthesized in the presence of 19.6% of Sn(acetate)$_4$, therefore it would be interesting to examine the photophysical properties of the isolated nanoclusters as a function of their size. The energy dispersive X-ray spectroscopy (EDS) analysis confirms the presence of Sn in purified In_2O_3 nanocluster samples (**See Figure S1**). The Sn% in 1.3, 1.5, and 1.7 nm In_2O_3 nanoclusters are 9.7, 12.2, and 14.4, respectively. To our surprise, none of the nanoclusters displayed LSPR properties, which is common for Sn-doped In_2O_3 NCs,[20] in the UV-Vis-NIR region (**Figure 3A**). Additionally, the optical band-gap of (E_g) ultrasmall In_2O_3 nanoclusters are determined from the Tauc plot considering In_2O_3 is an n-type

direct band-gap semiconductor. As illustrated in **Figure 3B**, the E_g of 1.3, 1.5, and 1.7 nm In_2O_3 nanoclusters are found to be 5.55, 5.64, and 5.75 eV, respectively. This exceptionally large E_g value is not unusual considering ultrasmall CdSe nanoclusters displayed Eg of ~4.0 eV whereas Eg of bulk CdSe is 1.7 eV.[46] The trend of E_g clearly follows the quantum confinement effect. Importantly, the E_g of the ultrasmall nanoclusters is significantly higher energy than the 3.0 eV reported band-gap of bulk, rh- In_2O_3.[47] To further evaluate the E_g of ultrasmall In_2O_3 nanoclusters, we compare our results with the theoretical effective mass approximation (EMA), Eq. 1.[37]

$$E_g(nanocluster) = E_g(bulk) + \frac{h^2}{8r^2}\left[\frac{1}{m_e^*} + \frac{1}{m_h^*}\right] - \frac{1.78e^2}{4\pi\varepsilon\varepsilon_0 r} \qquad \text{Eq. 1}$$

Where r is the radius of nanoclusters, m_e^* and m_h^* are the reduce mass of an electron and a hole, respectively, ($m_e^* = 0.3\ m_o$ and $m_h^* = 0.6\ m_o$, m_o = free electron mass), ε_o and ε are the permittivity of free space and relative permittivity (dielectric) of In_2O_3

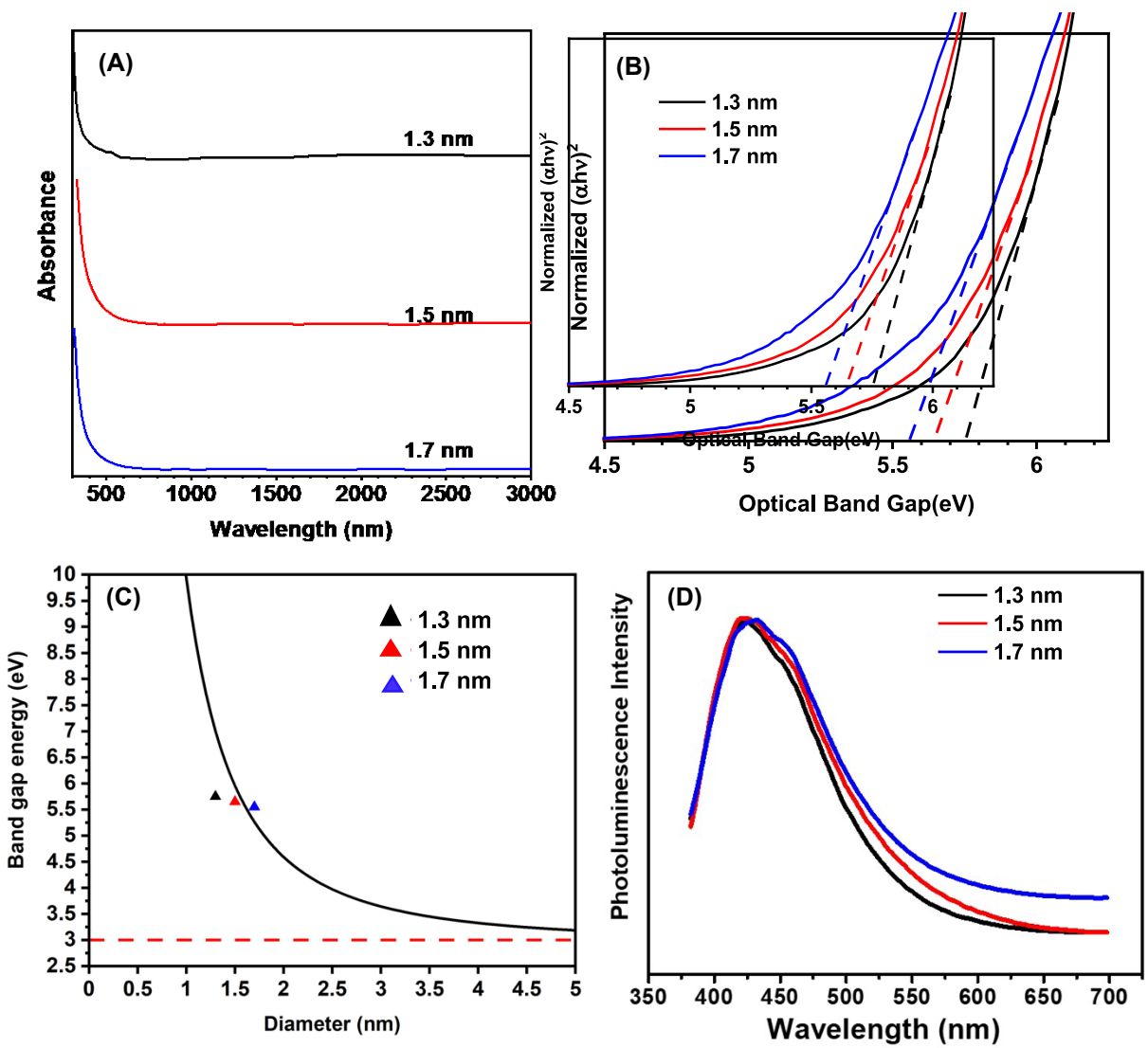

Figure 3. *(A) UV-Vis-NIR spectra of Sn-decorated ultrasmall In_2O_3 nanoclusters of different sizes. (B) The Tauc plot for direct band gap determination of the ultrasmall Sn-decorated In_2O_3 nanoclusters varying sizes. (C) Comparison of EMA-based calculated band gap energy (black line) and experimentally determined values for 1.3, 1.5, and 1.7 nm diameter (triangles). (D) PL emission spectra of In_2O_3 nanoclusters as a function of size. PL spectra were collected at 360 nm excitation wavelength. All optical spectra were collected at room temperature.*

(9.0),[48] respectively, and *e* is the elementary charge. As illustrated in **Figure 3C**, there is a very good correlation between experimentally determined E_g and the EMA prediction suggesting that the diameter of ultrasmall In_2O_3 nanoclusters can be established by comparing the EMA calculation results with the E_g. Together, ultrasmall In_2O_3 nanoclusters are wide band-gap semiconductors with an Eg comparable to diamond (~5.5 eV), thus these nanoclusters should be useful for high performance optoelectronic devices.[49]

At 360 nm excitation wavelength, the photoluminescence (PL) emission spectra of In_2O_3 nanoclusters show a broad peak centered around 430 nm (2.9 eV) with a long tail covering much of the visible region (**Figure 3D**). Interestingly, the PL peak maximum of ultrasmall In_2O_3 nanoclusters is significantly red-shifted in comparison to >4.0 nm diameter In_2O_3 and/or Sn:In_2O_3 NCs.[50] Therefore, we believe that the broad PL emission peak and an extremely large bathochromic shift (UV-Vis band gap – PL emission peak position) of 2.6 eV is due to the trap states related PL emission. We believe Sn:In_2O_3 NCs contain surface and/or deep trap states. As mentioned before, >80% atoms reside on the surface of ultrasmall (<2.0 nm) nanoclusters, therefore, any un-passivated surface metal sites create unwanted trap states. Moreover, any oxygen vacancies could create trap states. Nevertheless, holes from photoexcitation can be trapped in those states and recombined with electrons producing a broad PL peak. The trap state-related broad PL signature of ultrasmall semiconductors is well documented in the literature.[4, 51] Perhaps, an appropriate surface passivation of the ultrasmall nanoclusters could limit the formation of these trap states by filling them with the electron density of the ligand and thus not allowing the excited electrons to recombine into trap states before returning to their ground state.

Structural Analysis of Sn-Decorated In_2O_3 Nanoclusters: As described above, EDS analyses confirms the presence of Sn in ultrasmall In_2O_3 nanoclusters. We further characterized In_2O_3 nanoclusters with X-ray photoelectron spectroscopy (XPS). **Figure 4A,B** shows XPS spectra of In and Sn 3d regions. Characteristic In $3d_{5/2}$ and $3d_{3/2}$ peaks at 445.5 and 453.1 eV, respectively, appear. Shoulders present at ~446.5 and 454.5 eV are due to the formation of In^{+1} on the surface of the ultrasmall nanoclusters. This can be attributed to the oxygen vacancies donating electrons to the In^{3+} centers and reducing the terminal In^{3+} atoms to In^{+1}. The In $3d_{5/2}$ and $3d_{3/2}$ peak position of In_2O_3 nanoclusters containing 14.4% Sn matches well with ultrasmall, In_2O_3 nanoclusters without the Sn. The 1.7 nm In_2O_3 nanoclusters containing 14.4% Sn clearly show Sn $3d_{5/2}$ and $3d_{3/2}$ peaks with binding energies of 487.1 and 495.3 eV, respectively, that support the presence of Sn^{4+} and no metallic Sn^0 or Sn^{2+}. [52] Similar Sn $3d_{5/2}$ and $3d_{3/2}$ peaks are observed in 1.5 and 1.3 nm nanoclusters. Together, EDS and XPS analyses unequivocally support the presence of Sn in ultrasmall In_2O_3 nanoclusters. Therefore, it is quite intriguing that nanoclusters do not display LSPR properties.

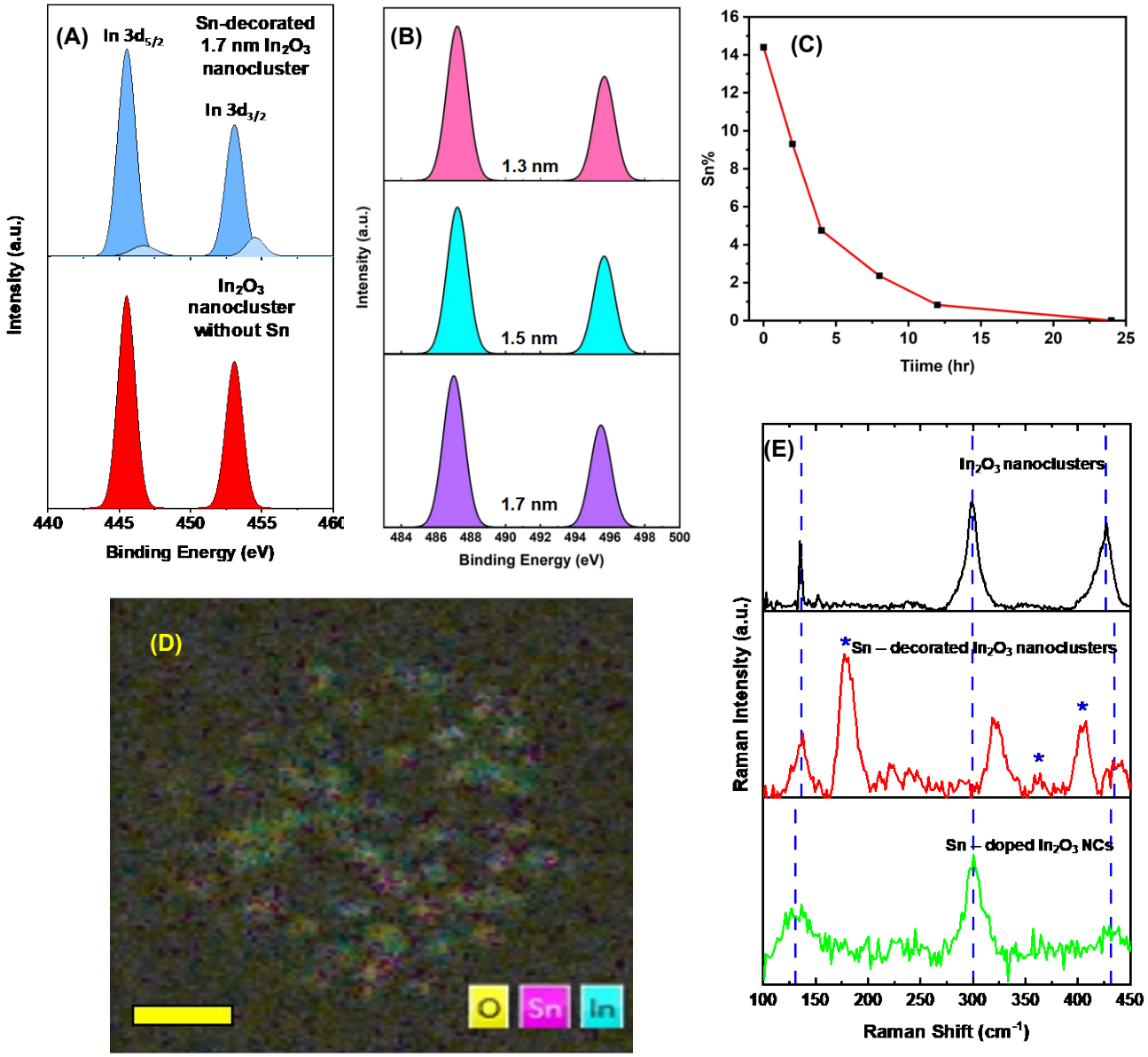

Figure 4. *(A) XPS spectra of In_2O_3 nanocrystals 0% (Red) and 19.6% (Blue) Sn: In(acac)$_3$ added to the reaction matrix. Binding energies of 445.6 eV for In $3d_{5/2}$ and 453.5 eV for In $3d_{3/2}$ (B) Sn 3d XPS spectra of 1.3 nm, 1.5 nm, and 1.7 nm respectively. For Sn 3d, peaks are present at binding energies of 495.6 eV for Sn $3d_{3/2}$ and 487.1 eV for Sn $3d_{5/2}$. (C) TMEDA ligand exchange showing Sn% as a function of time. (D) Energy dispersive X-ray image of 1.7 nm ultrasmall nanoclusters. The scale bar is 5 nm. (E) Raman spectrum of ultrasmall In_2O_3 nanoclusters (top) Sn-decorated ultrasmall In_2O_3 nanoclusters (middle) and Sn:In_2O_3 NCs (Bottom)*

To better understand this observed phenomenon we employed high-angle annular dark-field scanning transmission microscopy (HAADF-STEM) imaging and elemental mapping, see **Figure 4D** and **Figure S2**. The composition distribution of In_2O_3 nanoclusters clearly shows Sn is homogeneously distributed throughout the 1.7 nm In_2O_3 nanoclusters; however, it is difficult to ascertain whether Sn^{4+} ions incorporate in the In_2O_3 crystal lattice or reside onto the In_2O_3 surface as a Z-type ligand on the surface forming a strong metal-metal interaction.

We believe one of the following two plausible mechanisms may influence such unusual photophysical properties.

(1) Donor activation energy: In extrinsically doped metal oxides specifically, Sn-doped In_2O_3, it is critically important to match or at least be in close proximity of the energy levels between donor Sn^{4+} and conduction band of In_2O_3. The energy level of donor Sn^{4+} could be lower than the conduction band minima of extremely large band-gap (~5.5 eV) of ultrasmall In_2O_3 nanoclusters, therefore the activation energy for the electron transfer in the conduction band is reasonably high resulting in extremely low free electron concentrations and the lack of LSPR properties.[53] The elemental analysis support a significant amount of Sn (14.4%) in 1.7 In_2O_3 nanoclusters. Thus, it is reasonable to expect at least a weak LSPR signature in the optical spectrum instead of being completely non-LSPR (**Figure 3A**).

(2) Sn-decorated In_2O_3 nanoclusters. The alternative, and most likely mechanism involves presence of Sn^{4+} on the surface of ultrasmall In_2O_3 nanoclusters, instead of being incorporated into the In_2O_3 crystal as an extrinsic dopant. Under this condition, no LSPR response is expected. The ultrasmall In_2O_3 nanoclusters belong to hexagonal crystal family where In^{3+} resides in the center of the hexagonal closed-packed oxygen atoms.[54] The primary change during the phase change from rhombohedral to the cubic bixbyite (the potentially LSPR active phase) is the position of the anions (oxygen), specifically there are less anions between metal sites within the lattice; this means that introduction of a cation causes repulsive forces to increase as the dopant ion enters which generally

results in amorphous particle formations.[55] It is found in that even at high temperatures >800 °C that addition of high molar percent of Sn^{4+} the sample exhibited high resistivity which is likely a result of the formation of amorphous particles rather than an extrinsically doped structure.[56] Furthermore, the reaction between $Sn(acetate)_4$ and MA would form $Sn(acetate)_{4-x}(MA)_x$ that can act as an electron accepting Z-type ligand,[57] which is capable of interacting with surface oxygen atoms of the In_2O_3 crystal through coordination-type bonding. Together, we believe that the interaction between the $Sn(acetate)_{4-x}(MA)_x$ and In_2O_3 forms *"Sn-decorated In_2O_3 nanoclusters."*

To validate this prediction, we performed ligand-stripping experiments and further spectroscopy and microscopy characterizations. Briefly, *N*,*N*,*N*′,*N*′-tetramethylethane-1,2-diamine (TMEDA) is known to form metal complexes and strip Z-type ligands from the surface of ultrasmall semiconductor nanoclusters.[8] Ultrasmall, 1.7 nm In_2O_3 nanoclusters and TMEDA were stirred overnight and during that time period, a fixed volume of aliquot was removed at different points in time to analyze the In:Sn percentage in the purified nanoclusters by EDS (**Figure S3**). As shown in **Figure 4C**, the Sn% decreases overtime and only a negligible percentage of Sn is present after 24 hr of the reaction. This result supports Sn-decoration rather than Sn incorporation because if the Sn atoms are covalently bound to the In_2O_3 lattice structure, it would be extremely difficult to remove the covalent interaction through TMEDA treatment at room temperature. Therefore, it is expected that the TMEDA treatment should not alter the size and/or crystal structure of ultrasmall 1.7 nm In_2O_3 nanoclusters. To ensure no changes occurred, TEM analysis was performed on the 24 hr sample, that supports the presence of ultrasmall nanoclusters of ~1.7 nm (**Figure S4A**). The appearance of aggregated nanoclusters is due to the ligand stripping either by TMEDA treatment and/or solvent-assisted precipitation and purification. The XRD pattern of the same sample matches with the rh- In_2O_3 structure and 1.7 nm In_2O_3 nanoclusters without TMEDA treatment (**Figure S4B**).

We performed Raman spectroscopy analysis to further evaluate the structure of non-LSPR, ultrasmall nanoclusters and LSPR-active, Sn:In_2O_3 NCs. ~5.5 nm Sn:In_2O_3 NCs, which were synthesized according to the literature procedure described by Garcia et al.[38] See Experimental Section and **Figure S5**. **Figure 4E** illustrates the Raman spectra of ~1.8 nm In_2O_3 nanoclusters (without Sn), 1.7 nm Sn-decorated In_2O_3 nanoclusters, and 5.5 nm Sn:In_2O_3 NCs at room temperature. It is evident from our study that the Raman stretches of ultrasmall Sn-decorated nanoclusters and Sn:In_2O_3 NCs are not identical. Three major observations can be made: (1) The phonon vibration modes of In-O bond at 136, 300, and 426 cm^{-1} are much sharper and higher intensity in without-Sn and Sn-decorated In_2O_3 nanoclusters in comparison to Sn:In_2O_3 NCs where broad and relatively less intense stretches are observed. The broadening of Raman stretches represent the decrease of phonon correlation length as a consequence from the doping, which increases the disorder in the local crystal lattice. (2) The Raman stretch of (undoped) ultrasmall In_2O_3 nanoclusters and Sn:In_2O_3 NCs at 300 cm^{-1} moves to 321 cm^{-1} for Sn-decorated In_2O_3 nanoclusters. This higher energy shift could be due to lattice strain from the adsorption of Sn-complex onto the surface of 1.7 nm ultrasmall nanoclusters, as similar to adsorption of Z-type ligands onto ultrasmall/ultrathin CdSe nanoclusters/nanoplatelets.[58] (3) Additional Raman stretches at 179, 361, and 428 cm^{-1} are present in the Sn-decorated In_2O_3 nanoclusters which do not appear in either undoped In_2O_3 nanoclusters or Sn:In_2O_3 NCs. We predict these new stretches are associated with Sn-complexes that are bound to the In_2O_3 nanocluster surface.

To validate the prediction, we performed time-dependent density functional theory (TDDFT) calculations of a small fragment of In-O cluster bound to a Sn-carboxylate complex (**Figure S6**). The Raman stretch at 179 cm^{-1} can be assigned to In-O-Sn rocking mode, whereas carboxylate oxygen bound to Sn shows Sn-O stretch at 363 cm^{-1}. Finally, interaction between In_2O_3 surface and Sn appears as a O-Sn scissoring mode at 405 cm^{-1}. Importantly, In-O-Sn and O-Sn stretches should not be present in a Sn-carboxylate complex. Therefore, we performed the Raman analysis of solid Sn(acetate)$_4$. Indeed, these two stretches are absent and only the appearance of Sn-O (from carboxylate) stretch at ~371 cm^{-1} (**Figure S7**) is witnessed. The observed, slight differences in the peak position between experimental and DFT-calculated

spectra due to local environment where Sn-decorated In_2O_3 nanoclusters were analyzed as a solid film whereas gas-phase calculations were conducted for the In_2O_3-Sn-carboxylate complex. Together, the Raman results suggest that the local symmetry of ultrasmall nanoclusters (undoped) is different than Sn:In_2O_3 NCs, and further support our argument of the presence of Sn-decorated In_2O_3 nanoclusters.

Mechanism of Ultrasmall Sn-Decorated In_2O_3 Nanocluster Formation: High quality metal oxide NCs can be synthesized via hydrolysis of metal carboxylate complexes at an elevated temperature (>250 °C).[59] The water molecules are homogeneously produced in the reaction mixture either by the esterification reaction between carboxylate and alcohol group or via amine and acid condensation reactions. We propose the following mechanism whereby addition of OLAm into metal precursors leads to the formation of ultrasmall nanoclusters. Addition of MA to ($In(acac)_3$) in ODE at 130 °C would allow to form $In(acac)_{3-x}(MA)_x$ complexes. Injection of OLAm at 290 °C allows in-situ formation of water molecules resulted from the condensation reaction between aliphatic carboxylic acid and amine (**Scheme 1**). The hydrolysis of $In(acac)_{3-x}(MA)_x$ by water molecules leads to the formation of In_2O_3 monomers which eventually undergo growth processes to form ultrasmall nanoclusters. We believe that the formation of ultrasmall In_2O_3 nanoclusters is a kinetically controlled process where the concentration of passivating ligands in the reaction mixture dictates the size, as well as the LSPR properties of final nanoclusters/NCs.

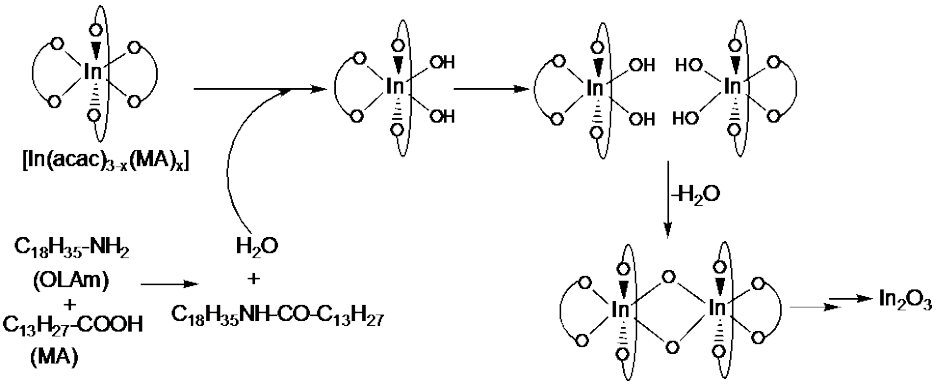

Scheme 1. Proposed Mechanism for the Formation of Ultrasmall Sn-decorated In_2O_3 Nanoclusters

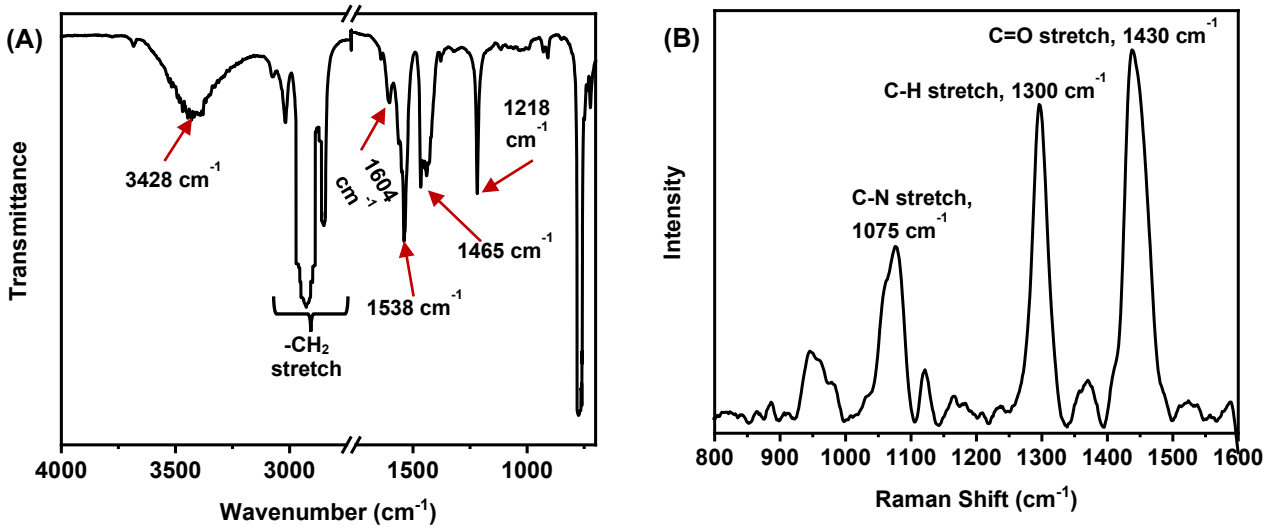

Figure 5. *(A) FTIR and (B) Raman spectra of ultrasmall Sn-decorated In_2O_3 nanoclusters.*

We analyzed purified and isolated, ultrasmall In_2O_3 nanoclusters by FTIR and Raman spectroscopy to determine their surface ligand chemistry. **Figure 5A** illustrates the IR stretches of ligand-passivated nanoclusters where a broad peak at 3334 cm^{-1} and a strong peak at 1538 cm^{-1} are assigned as N-H bending modes of primary amine moiety of OLAm.[60-61] The C-N stretch of amine appears at 1218 cm^{-1}.[60-61] The symmetric (1465 cm^{-1}) and asymmetric (1604 cm^{-1}) stretching represents vibrations of $-COO^-$.[62] A separation of 139 cm^{-1} between these two stretching modes suggests bidentate chelating In-OOC-R (In-myristate) binding.[63] Peaks ~2800-3000 cm^{-1} are due to strong C-H stretches of $(CH_2)_n$- backbone of myristate and OLAm. In the Raman spectrum, strong peaks at 1075 cm^{-1} and 1430 cm^{-1} are assigned to C-N and C=O stretches of OLAm and myristate, respectively (**Figure 5B**).[64-65] Small peaks in the C=O region could be associated with $Sn(acetate)_{4-x}(MA)_x$. The Raman stretch at 1300 cm^{-1} appears due to the vibration of $-CH_2$, which is closer to the carboxylate group.[65-66] Importantly, the Raman stretches of ligands appear to be sharper. This sharpness of the peak indicates highly ordered ligand packing on the surface of nanoclusters.[67] Perhaps, long aliphatic chain of MA could form interdigitated bilayer structures due to hydrophobic-

hydrophobic and van der Waals interactions between hydrocarbon chains.[62, 68] Together, our spectroscopy analyses suggest that the surface of ultrasmall In_2O_3 nanoclusters is passivated with mixed ligands, OLAm and myristate.

The surface ligand chemistry substantially controls the nucleation and growth processes of inorganic NCs by manipulating the surface energy.[62, 69-70] We used a large excess of MA in the reaction mixture, therefore tight ligand packing – as evident due to the appearance of sharp Raman stretches –stabilizes the crystal lattice via lowering the surface energy of the ultrasmall nanoclusters; as well as creates thick barrier for monomers to diffuse to the surface of the nanoclusters for the further growth. This observation is further supported by formation of smaller and smaller nanoclusters with increasing concentrations of MA in the reaction mixture (see Table S1). Our results are in agreement with the literature where an increase of metal-to-ligand mole ratio produces smaller nanoclusters.[71] To prove our hypothesis of kinetically controlled formation of nanoclusters, we performed the same nanocluster synthesis using 3.75 mmol of MA while keeping concentrations of all other reagents identical. Interestingly, the purified sample shows the presence of both ultrasmall nanoclusters (~1.8 nm) and ~3.0 nm NCs (**Figure S8A**). The colloidal dispersion of the sample displays LSPR properties (**Figure S8B**). We believe that 3.75 mmol of MA is insufficient to form a tight packing on the surface of ultrasmall nanoclusters to prevent the further diffusion of monomers to continue the growth process. Under such circumstances, larger, LSPR active NCs are formed because of Sn doping (Sn:In_2O_3 NCs). It has been suggested in the literature that dopant cations can control the growth of metal oxide NCs.[54] We believe that the formation of ultrasmall, Sn-decorated In_2O_3 nanoclusters is mostly controlled by the ligand and not Sn^{4+}. To further understand, in a control experiment 1.7 nm In_2O_3 nanoclusters are formed when 4.0 mmol of MA was used without the addition of Sn(acetate)$_4$, see **Figure S9**. At ultrasmall size range, >80% of atoms are at the surface, thus any unpassivated atoms would increase the surface energy. It is necessary to passivate most of the surface atoms to reduce the free energy of the surface of the ultrasmall nanoclusters. Although ultrasmall In_2O_3 nanoclusters could grow to larger NCs at 230 °C,[72] we do not observe any size change even after heating the reaction mixture at this temperature for an additional 1 hr (data not shown). Thus,

we believe that during the annealing at 230 °C, ultrasmall nanoclusters are forced into a status of equilibrium of Sn-decoration on the surface to lower the surface energy that may provide additional stability and prevent further growth. Together, our finding suggests that the In-to-ligand mole ratio is critical to control the kinetically driven formation steps and to obtain nearly monodisperse single size nanoclusters.

Scheme 2. *Reaction Conditions for the Seeded Growth Synthesis of Plasmonic Sn:In_2O_3 Nanostructures Utilizing Ultrasmall Sn-Decorated In_2O_3 Nanoclusters.*

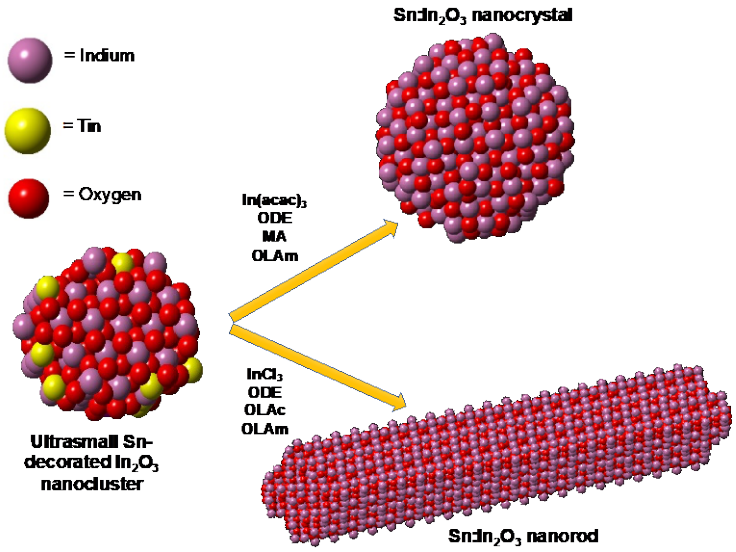

Preparation of Plasmonic Sn:In_2O_3 NCs Using Ultrasmall Sn-Decorated In_2O_3 Nanocluster Seeds. Seeded-growth synthesis of noble metal NCs is well-established;[73] morphological control of the seeds, chemical structure of metal precursor and surface passivating ligands in growth solution, as well as the reagent concentrations in the reaction condition dictate the size and shape of final NCs and their LSPR properties. In terms of metal-oxide NCs, Hutchison and coworkers reported a "*living chain-growth polymerization*"[74] type approach to synthesize various types metal-oxide NCs. They have shown that the ex-situ addition of metal precursors in metal-oxide NC growth solutions allow continuous growth where the nuclei attach onto growing NCs.[75] To the best of our knowledge, however no studies have been conducted where isolated, ultrasmall metal-oxide nanoclusters used as seeds to grow larger spherical and/or

anisotropically-shaped metal-oxide NCs. As shown in **Scheme 2**, we sought to investigate the growth of Sn:In_2O_3 NCs through controlled addition of In-precursors in a solution of 1.7 nm, Sn-decorated In_2O_3 nanoclusters without the addition of Sn-precursors. Briefly, 30 mg of purified Sn-decorated In_2O_3 nanoclusters were mixed with MA and OLAm in ODE along with a specific amount of $In(acac)_3$ (see Table 1). The reaction mixture was heated at a specific temperature to synthesize Sn:In_2O_3 spherical NCs. The purified NCs were characterized by TEM to determine the size and dispersity. **Figure 6A-F** illustrates TEM images and corresponding histograms of the NCs. As expected from the continuous growth, NCs grow in larger sizes with increasing concentrations of $In(acac)_3$ in the reaction condition.

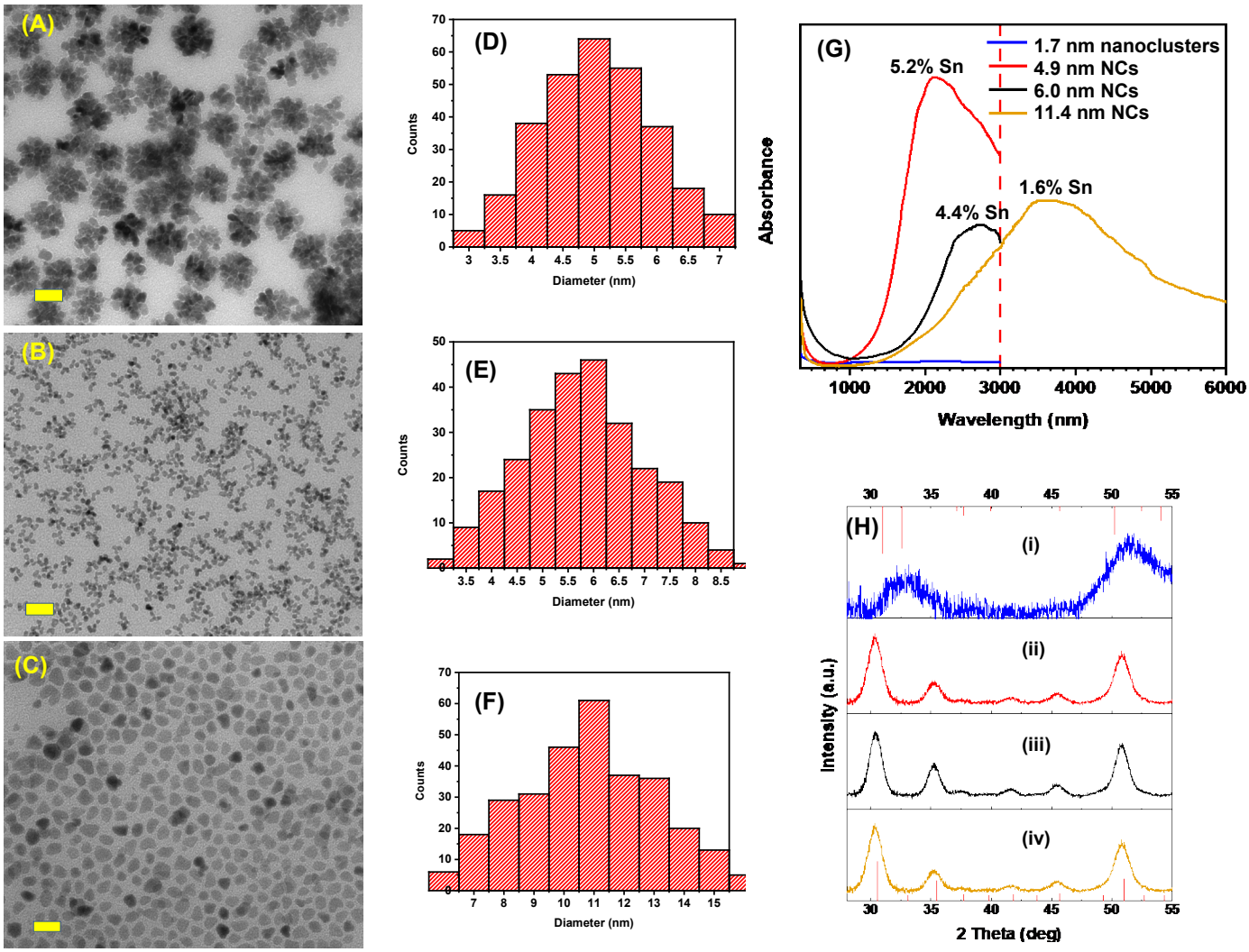

Figure 6. *TEM images of plasmonic Sn:In_2O_3 NCs synthesized using 0.036 (A), 0.07 (B), and 0.14 (C) mmol of $In(acac)_3$. Corresponding histograms of size analysis are shown in (D)-(E). (G) UV-Vis-NIR spectrum of Sn:In_2O_3 NCs varying sizes. The spectrum was collected in CCl_4 at room temperature. (H) XRD patterns of ultrasmall Sn-decorated In_2O_3 nanoclusters (i), and plasmonic 4.9 (ii), 6.0 (iii) and 11.4 nm Sn:In_2O_3 NCs. XRD pattern of rh- (top, JCPDS 21-0406) and c-In_2O_3 (bottom, JCPDS 06-0416) are shown as references.*

We are able to synthesize 4.9, 6.0, and 11.4 nm NCs by adding 15, 30, and 60 mg of $In(acac)_3$, respectively. EDS analysis of purified NCs shows the presence of Sn where the smallest NCs contain the highest % and vice versa. This result is in agreement with the experimental parameters because no extra Sn was added in the reaction mixture, whereas number of In atoms in the NC increases as the size increases. XRD patterns of 4.9 and 11.4 nm Sn:In_2O_3 NCs show peaks associated with (400), (431), (440), and (622) facets that match with the pattern of bulk, cubic bixbyite (bcc)-In_2O_3, see **Figure 6H.** Clearly, there is a phase transformation from ultrasmall Sn-decorated In_2O_3 nanoclusters to larger Sn:In_2O_3 NCs. We believe that multiple washing of ultrasmall Sn-decorated In_2O_3 nanoclusters removes most of the surface passivating ligands that allows anions from the metal precursor to be adsorbed on the surface. This creates surface strain that facilitate the transformation of metastable rh-In_2O_3 to bcc-In_2O_3 to promote the growth process.

At a lower In-precursor concentration, three-dimensional arrangement of “flower-like” nanostructures are observed where individual NCs are connected to each other (**Figure 6A and S10**). We are not certain what could cause this type of higher-order organization process but could predict that hydrophobic tails of passivating ligands induce hydrophobic-hydrophobic and van der Waals interactions in non-polar organic solvent (ODE) that promote the mesoscale assembly process.[76] It is important to mention that in the seeded-growth synthesis of spherical Sn:In_2O_3 NCs, very low concentrations of passivating ligands (15 mg of MA and 300 uL of OLAm) were used. Therefore, with increasing In-precursor concentration larger NCs are formed, and their surface may not be fully passivated due to lack of passivating ligands. Under such

circumstance, hydrophobic-hydrophobic and van der Waals interactions are negligible resulting in appearance of individual NCs. We also hypothesize that the extremely low concentration of passivating ligands in the reaction condition unable to stabilize the ultrasmall nanoclusters that in turn facilitate the attachment of monomers and lead to larger NCs.

Table 1. Summary of synthetic parameters and structural and plasmonic properties of $Sn:In_2O_3$ NCs.

In-precursor	In-precursor amount mg (mmol)	Sn% in NCs	size of NCs (nm)	LSPR peak position (nm)	Ne value (cm^{-3})
$In(acac)_3$	15 (0.036)	5.2	Spherical 4.9 ± 0.9	2130	1.22×10^{20}
$In(acac)_3$	30 (0.070)	4.4	Spherical 6.0 ± 1.2	2725	1.10×10^{20}
$In(acac)_3$	60 (0.140)	1.6	Spherical 11.4 ± 2.3	3650	9.65×10^{19}
$InCl_3$	40 (0.180)	7.3	Rod length (19.8) x diameter (2.0)	1825	5.31×10^{19}

$Sn:In_2O_3$ NCs were characterized either by UV-Vis-NIR and FTIR spectroscopy to evaluate their optoelectronic properties. Spherical 4.9, 6.0, and 11.4 nm NCs display LSPR peaks at 2130, 2725, and 3650 nm, respectively. The LSPR peak position is in agreement with the Sn% presented above where the LSPR peak undergoes a graduate red-shift as the Sn% in the NC decreases. Importantly, we are able to tune the LSPR

peak position of Sn:In_2O_3 NCs in the entire NIR region of the solar spectrum by changing the size of NCs. We further calculate the free carrier density (N_e) of Sn:In_2O_3 NCs by utilizing the empirical Drude approximation theory (Eq. 1 and 2)[77-78] where ω_{LSPR} is the LSPR frequency, ω_p is the bulk plasma oscillation frequency of electrons for In_2O_3, ε_∞ is the high frequency dielectric constant of In_2O_3, and $\varepsilon_r = -\kappa\varepsilon_m$. κ is shape factor of the NCs. For spherical NCs this value is 2 due to the spherical geometry of the NCs and γ is the bulk collision frequency determined from the LSPR peak.

$$\omega_{LSPR} = \sqrt{\frac{\omega_p^2}{\varepsilon_\infty - \varepsilon_r} - \gamma^2} \qquad \text{Eq. 1}$$

$$\omega_p^2 = \frac{N_e e^2}{\varepsilon_0 m_e} \qquad \text{Eq. 2}$$

Finally, N_e can be calculated by solving Eq. 2 with the consideration that the bulk refractive index is 2.24 from CCl_4. N_e values for three different sizes NCs are summarized in Table 1. The calculated N_e value of our Sn:In_2O_3 NCs is in agreement with the literature.[79]

Previously, Murray and coworkers demonstrated that the shape of TiO_2 NCs can be controlled via a seeded-growth method by systematic manipulation of metal precursors and choice of organic surface passivating ligands.[80] As a proof-of-concept, under optimized reaction conditions, we used Sn-decorated In_2O_3 nanoclusters along with $InCl_3$, and mixed passivating ligands, oleic acid (OLAc) and OLAm. A detailed synthetic method is provided in the Experimental Section. Low resolution TEM analysis (**Figure 7A-C**) reveals for formation of ultrathin nanorods with 20 nm in length and having a diameter of 2 nm. As illustrated in **Figure 7D**, the nanorod sample display a XRD pattern that matches with bcc-In_2O_3 structure with strong diffraction of (400), (431), (440), and (622) facets. EDS analysis supports the presence of Sn with 7.3% doping. The optical characterization of Sn:In_2O_3 nanorods display an LSPR peak ~1750 nm (**Figure 7E**). We also calculated the N_e value by using the correct shape factor for one-dimensional nanorods (see Supporting Information) and determined to be 5.31 x 10^{19} cm^{-3}. We propose that OLAc binds onto ultrasmall NC surface and act as a facet blocking agent, resulting in attachment of monomers through oriented attachment along the (104) facet of ultrasmall nanoclusters. Surprisingly, the diameter of nanorods is close to the size of ultrasmall nanoclusters that suggest preferential and unidirectional

growth of nanorods. We should also mention that there could be alternative mechanisms for the formation of nanorods under our experimental conditions: (i) $InCl_3$ produces chloride ion in the solution that can be adsorbed onto ultrasmall NC surface and create local dipole moment. Therefore, dipole-dipole interactions between nanoclusters could lead to oriented attachment and formation of one-dimensional nanorods. (ii) The formation of In-oleate complex produces HCl, which would change the solution pH and thus the growth conditions. Nevertheless, this is the first example where plasmonic $Sn:In_2O_3$ nanorods are synthesized via a colloidal-based seeded growth approach. We are actively working to synthesize various anisotropic shapes, plasmonic $Sn:In_2O_3$ NCs by manipulating the seeded growth conditions.

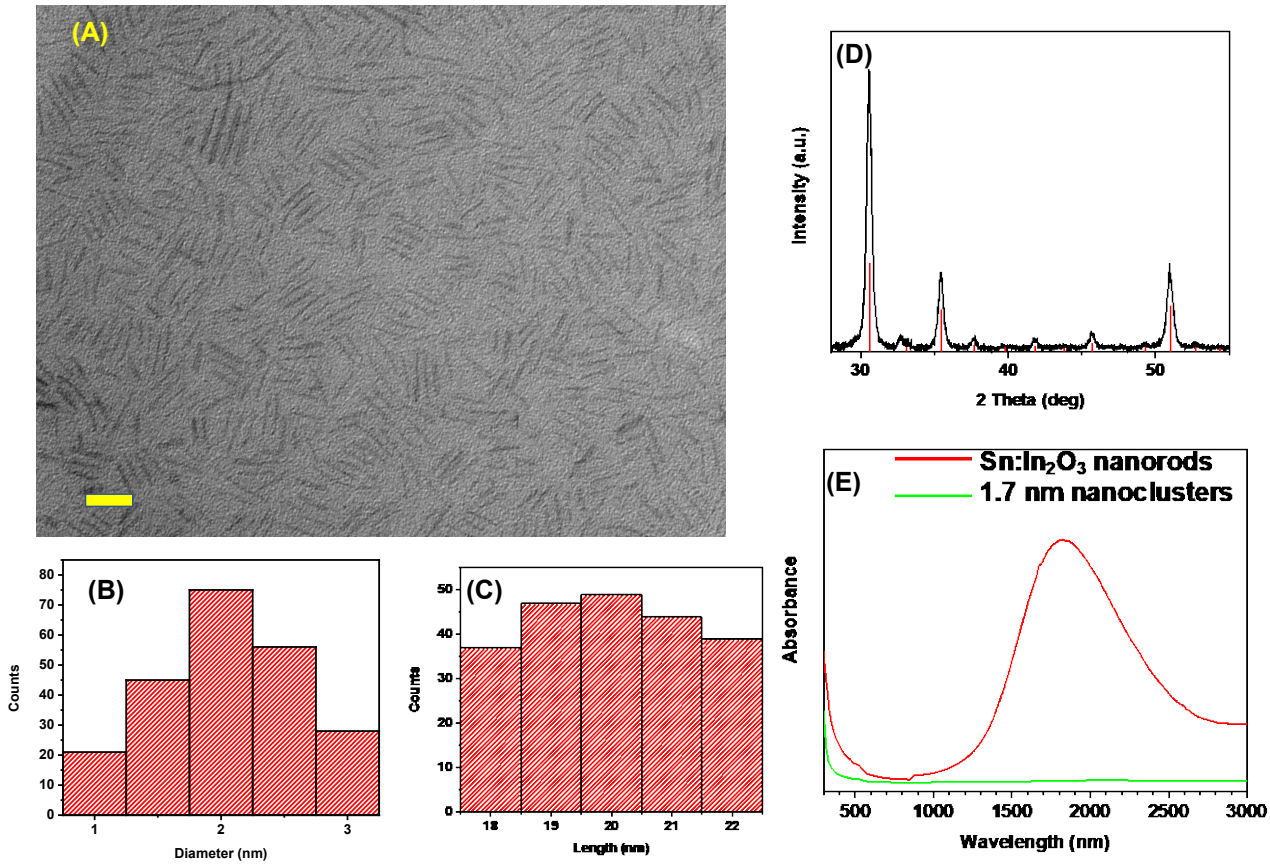

Figure 7. *(A) Low magnification transmission electron micrograph of $Sn:In_2O_3$ nanorods. The scale bar is 20 nm. Histograms of diameter (B) and length (D) of $Sn:In_2O_3$ nanorods. (D) The XRD pattern of nanorods. C-In_2O_3 standard is shown at the bottom (JCPDS 06-0416). (E) UV-*

Vis-NIR spectrum of Sn:In_2O_3 nanorods. The spectrum was collected in CCl_4 at room temperature.

In summary, there are several important aspects of our seeded-growth synthesis of Sn:In_2O_3 NCs: (i) The spherical NCs and/or one-dimensional nanorods were synthesized without the addition of any Sn-precursors. This suggests the presence of Sn^{4+} in the reaction media where Sn^{4+} ions can be enveloped during the growth process and act as extrinsic dopants to ultimately produce observed LSPR properties of the resulting NCs/nanorods. (ii) Sn-decorated In_2O_3 nanocluster seeds retain their reactivity to induce further growth and allow interstitial doping. (iii) The LSPR active NC synthesis follows the living chain growth polymerization approach where monomers in the reaction mixture continuously feed the growing NCs until all the metal precursors are completely converted to monomers and consumed. Therefore, it is expected that even larger size, spherical NCs can be synthesized either by using higher concentrations of In-precursors or continuous injection of metal precursors. (iv) It is also important to mention that the 1.5 nm Sn-decorated In_2O_3 nanocluster seeds do not grow to larger NCs under reaction identical conditions as 1.7 nm seeds. This could be due to extremely high thermodynamic stability of 1.5 nm nanoclusters as similar to extremely high stability of magic-sized $(CdSe)_{34}$ nanoclusters. Although the concept of metal-oxide magic-sized nanoclusters has never discussed in the literature, it is possible that they could exist as similar to metal chalcogenide and noble metal nanoclusters.[11]

Conclusions

We have developed a colloidal synthetic strategy to prepare, nearly monodisperse, metastable, ultrasmall Sn-decorated In_2O_3 nanoclusters. The findings show that the concentration of surface passivating ligands and annealing process are extremely crucial to synthesize such nanoclusters. We have characterized the optoelectronic properties of Sn-decorated In_2O_3 nanoclusters and found that the experimental and EMA theory-based band gaps match extremely well. HAADF-STEM, XPS, and Raman analyses support the formation of Sn-decorated In_2O_3 nanoclusters where Sn-complex acts as an electron accepting Z-type ligands, which bind to In_2O_3 surface oxygen atoms. This electronic interaction is further supported by TDDFT

calculations showing new Raman stretches that are distinctly different from In_2O_3 nanoclusters and Sn:In_2O_3 NCs. Additional control experiments also support the argument of Z-type ligand attachment on the surface of In_2O_3 core. We believe that our synthetic method can be extended to other metal oxide (CdO, Gd_2O_3, etc.) nanocluster syntheses. Experimentally determined 5.5 eV optical band-gap of Sn-decorated In_2O_3 nanoclusters is truly a key signature of wide band-gap nanomaterials that could be useful for optoelectronic device fabrication.

For the first time, we have shown Sn-decorated In_2O_3 nanoclusters can be used as seeds for the synthesis of plasmonic Sn:In_2O_3 NCs, which are achieved by addition of In-precursor and passivating ligands without the addition of Sn-precursors in the seed solution. The amount of In-precursor used in the reaction mixture dictates the size, and thus the LSPR frequency of spherical Sn:In_2O_3 NCs. We hypothesize living chain growth polymerization as a model for the growth of ultrasmall nanoclusters into large NCs. Interestingly, the chemical structure of anions in In-precursors dictates the morphology of the Sn:In_2O_3 NCs. Through our seeded growth-based colloidal approach, plasmonic Sn:In_2O_3 nanorods are synthesized for the first time by using $InCl_3$ instead of $In(acac)_3$, which produces spherical NCs. Ultrathin diameter Nanorods with aspect ratio of 10.0 display a plasmon frequency in the NIR region with the N_e value of 5.31×10^{19} cm^{-3}. Future work will focus on the exploration of these high quality ultrasmall Sn-decorated In_2O_3 nanoclusters for synthesizing different anisotropic shapes Sn:In_2O_3 nanostructures displaying plasmonic properties and study their shape dependent LSPR properties. Finally, owing to facile charge separation in one-dimensional structure coupled with LSPR properties, we believe plasmonic Sn:In_2O_3 nanorods could be used as photocatalysts.

ASSOCIATED CONTENT

Supporting Information. Additional TEM images, experimental UV-Vis-NIR spectra and EDS spectra of In_2O_3 nanoclusters and NCs, theoretical Raman spectrum of Sn(acetate)$_4$, reaction table, and equations relevant to free electron density calculations.

ACKNOWLEDGMENT

This work was supported by the funding from the National Science Foundation grant (DMR-1747582). RS also thanks National Institute of Justice grant 2018-75-CX-0034 for the acquisition of the Raman microscope. XPS analyses were conducted at the Chapel Hill Analytical and Nanofabrication Laboratory, which is supported by the National Science Foundation grant, ECCS-2025064. We thank Dr. C. Donley for the assistance with the XPS analysis.

References

1. Jin, R.; Zeng, C.; Zhou, M.; Chen, Y., Atomically Precise Colloidal Metal Nanoclusters and Nanoparticles: Fundamentals and Opportunities. *Chem. Rev.* **2016,** *116* (18), 10346-10413.
2. Sardar, R.; Funston, A. M.; Mulvaney, P.; Murray, R. W., Gold Nanoparticles: Past, Present, and Future. *Langmuir* **2009,** *25* (24), 13840-13851.
3. Newton, J. C.; Ramasamy, K.; Mandal, M.; Joshi, G. K.; Kumbhar, A.; Sardar, R., Low-Temperature Synthesis of Magic-Sized CdSe Nanoclusters: Influence of Ligands on Nanocluster Growth and Photophysical Properties. *The Journal of Physical Chemistry C* **2012,** *116* (7), 4380-4389.
4. Bowers, M. J.; McBride, J. R.; Rosenthal, S. J., White-Light Emission from Magic-Sized Cadmium Selenide Nanocrystals. *Journal of the American Chemical Society* **2005,** *127* (44), 15378-15379.
5. Kim, B. H.; Hackett, M. J.; Park, J.; Hyeon, T., Synthesis, characterization, and application of ultrasmall nanoparticles. *Chem. Mater.* **2014,** *26* (1), 59-71.
6. Kuzume, A.; Ozawa, M.; Tang, Y.; Yamada, Y.; Haruta, N.; Yamamoto, K., Ultrahigh sensitive Raman spectroscopy for subnanoscience: Direct observation of tin oxide clusters. *Sci Adv* **2019,** *5* (12), eaax6455.
7. Teunis, M. B.; Dolai, S.; Sardar, R., Effects of Surface-Passivating Ligands and Ultrasmall CdSe Nanocrystal Size on the Delocalization of Exciton Confinement. *Langmuir* **2014,** *30* (26), 7851-7858.
8. Lawrence, K. N.; Dutta, P.; Nagaraju, M.; Teunis, M. B.; Muhoberac, B. B.; Sardar, R., Dual Role of Electron-Accepting Metal-Carboxylate Ligands: Reversible Expansion of Exciton Delocalization and Passivation of Nonradiative Trap-States in Molecule-like CdSe Nanocrystals. *Journal of the American Chemical Society* **2016,** *138* (39), 12813-12825.
9. Sau, T. K.; Murphy, C. J., Seeded high yield synthesis of short Au nanorods in aqueous solution. *Langmuir* **2004,** *20* (15), 6414-6420.
10. Pun, A. B.; Mule, A. S.; Held, J. T.; Norris, D. J., Core/Shell Magic-Sized CdSe Nanocrystals. *Nano Lett.* **2021,** *21* (18), 7651-7658.
11. Harrell, S. M.; McBride, J. R.; Rosenthal, S. J., Synthesis of Ultrasmall and Magic-Sized CdSe Nanocrystals. *Chem. Mater.* **2013,** *25* (8), 1199-1210.
12. Kudera, S.; Zanella, M.; Giannini, C.; Rizzo, A.; Li, Y.; Gigli, G.; Cingolani, R.; Ciccarella, G.; Spahl, W.; Parak, W. J., Sequential growth of magic-size CdSe nanocrystals. *Adv. Mater.* **2007,** *19* (4), 548-552.
13. Wang, Y.; Liu, Y. H.; Zhang, Y.; Wang, F.; Kowalski, P. J.; Rohrs, H. W.; Loomis, R. A.; Gross, M. L.; Buhro, W. E., Isolation of the Magic-Size CdSe Nanoclusters [(CdSe) 13 (n-octylamine) 13] and [(CdSe) 13 (oleylamine) 13]. *Angew. Chem. Int. Ed.* **2012,** *51* (25), 6154-6157.
14. Cossairt, B. M.; Owen, J. S., CdSe clusters: At the interface of small molecules and quantum dots. *Chem. Mater.* **2011,** *23* (12), 3114-3119.
15. Suzuki, T.; Watanabe, H.; Ueno, T.; Oaki, Y.; Imai, H., Significant Increase in Band Gap and Emission Efficiency of In2O3 Quantum Dots by Size-Tuning around 1 nm in Supermicroporous Silicas. *Langmuir* **2017,** *33* (12), 3014-3017.
16. Reghu, A.; LeGore, L. J.; Vetelino, J. F.; Lad, R. J.; Frederick, B. G., Distinguishing Bulk Conduction from Band Bending Transduction Mechanisms in Chemiresistive Metal Oxide Gas Sensors. *The Journal of Physical Chemistry C* **2018,** *122* (19), 10607-10620.
17. Mochizuki, D.; Kumagai, K.; Maitani, M. M.; Suzuki, E.; Wada, Y., Precise Control of Photoinduced Electron Transfer in Alternate Layered Nanostructures of Titanium Oxide–Tungsten Oxide. *The Journal of Physical Chemistry C* **2014,** *118* (40), 22968-22974.

18. Bhaskar, S.; Visweswar Kambhampati, N. S.; Ganesh, K. M.; P, M. S.; Srinivasan, V.; Ramamurthy, S. S., Metal-Free, Graphene Oxide-Based Tunable Soliton and Plasmon Engineering for Biosensing Applications. *ACS Applied Materials & Interfaces* **2021,** *13* (14), 17046-17061.
19. Crockett, B. M.; Jansons, A. W.; Koskela, K. M.; Johnson, D. W.; Hutchison, J. E., Radial dopant placement for tuning plasmonic properties in metal oxide nanocrystals. *ACS nano* **2017,** *11* (8), 7719-7728.
20. Kanehara, M.; Koike, H.; Yoshinaga, T.; Teranishi, T., Indium tin oxide nanoparticles with compositionally tunable surface plasmon resonance frequencies in the near-IR region. *Journal of the American Chemical Society* **2009,** *131* (49), 17736-17737.
21. Gordon, T. R.; Paik, T.; Klein, D. R.; Naik, G. V.; Caglayan, H.; Boltasseva, A.; Murray, C. B., Shape-dependent plasmonic response and directed self-assembly in a new semiconductor building block, indium-doped cadmium oxide (ICO). *Nano Lett.* **2013,** *13* (6), 2857-2863.
22. Erwin, S. C.; Zu, L.; Haftel, M. I.; Efros, A. L.; Kennedy, T. A.; Norris, D. J., Doping semiconductor nanocrystals. *Nature* **2005,** *436* (7047), 91-94.
23. Páez, A. M., Transition metal oxides: Geometric and electronic structures. *J. Chem. Educ.* **1994,** *71* (5), 381-388.
24. Liu, Z.; Zhong, Y.; Shafei, I.; Borman, R.; Jeong, S.; Chen, J.; Losovyj, Y.; Gao, X.; Li, N.; Du, Y., Tuning infrared plasmon resonances in doped metal-oxide nanocrystals through cation-exchange reactions. *Nature communications* **2019,** *10* (1), 1-11.
25. Maier, S. A., *Plasmonics: fundamentals and applications*. Springer: 2007; Vol. 1.
26. Kriegel, I.; Scotognella, F.; Manna, L., Plasmonic doped semiconductor nanocrystals: Properties, fabrication, applications and perspectives. *Physics Reports* **2017,** *674*, 1-52.
27. Staller, C. M.; Robinson, Z. L.; Agrawal, A.; Gibbs, S. L.; Greenberg, B. L.; Lounis, S. D.; Kortshagen, U. R.; Milliron, D. J., Tuning Nanocrystal Surface Depletion by Controlling Dopant Distribution as a Route Toward Enhanced Film Conductivity. *Nano Lett.* **2018,** *18* (5), 2870-2878.
28. Vaishnav, V.; Patel, P.; Patel, N., Preparation and characterization of indium tin oxide thin films for their application as gas sensors. *Thin Solid Films* **2005,** *487* (1-2), 277-282.
29. Martinez, M.; Herrero, J.; Gutierrez, M., Optimisation of indium tin oxide thin films for photovoltaic applications. *Thin Solid Films* **1995,** *269* (1-2), 80-84.
30. Shen, Z.; Burrows, P. E.; Bulovic, V.; Forrest, S. R.; Thompson, M. E., Three-color, tunable, organic light-emitting devices. *Science* **1997,** *276* (5321), 2009-2011.
31. Weaver, A. L.; Gamelin, D. R., Photoluminescence Brightening via Electrochemical Trap Passivation in ZnSe and Mn2+-Doped ZnSe Quantum Dots. *Journal of the American Chemical Society* **2012,** *134* (15), 6819-6825.
32. Kovalenko, M. V.; Manna, L.; Cabot, A.; Hens, Z.; Talapin, D. V.; Kagan, C. R.; Klimov, V. I.; Rogach, A. L.; Reiss, P.; Milliron, D. J.; Guyot-Sionnnest, P.; Konstantatos, G.; Parak, W. J.; Hyeon, T.; Korgel, B. A.; Murray, C. B.; Heiss, W., Prospects of Nanoscience with Nanocrystals. *ACS Nano* **2015,** *9* (2), 1012-1057.
33. Agrawal, A.; Cho, S. H.; Zandi, O.; Ghosh, S.; Johns, R. W.; Milliron, D. J., Localized surface plasmon resonance in semiconductor nanocrystals. *Chem. Rev.* **2018,** *118* (6), 3121-3207.
34. Dolai, S.; Dutta, P.; Muhoberac, B. B.; Irving, C. D.; Sardar, R., Mechanistic Study of the Formation of Bright White Light-Emitting Ultrasmall CdSe Nanocrystals: Role of Phosphine Free Selenium Precursors. *Chem. Mater.* **2015,** *27* (3), 1057-1070.
35. Glaser, T.; Müller, C.; Sendner, M.; Krekeler, C.; Semonin, O. E.; Hull, T. D.; Yaffe, O.; Owen, J. S.; Kowalsky, W.; Pucci, A.; Lovrinčić, R., Infrared Spectroscopic Study of Vibrational Modes in Methylammonium Lead Halide Perovskites. *The Journal of Physical Chemistry Letters* **2015,** *6* (15), 2913-2918.

36. Pun, A. B.; Mazzotti, S.; Mule, A. S.; Norris, D. J., Understanding Discrete Growth in Semiconductor Nanocrystals: Nanoplatelets and Magic-Sized Clusters. *Acc. Chem. Res.* **2021,** *54* (7), 1545-1554.
37. Brus, L., Electronic wave functions in semiconductor clusters: experiment and theory. *The Journal of Physical Chemistry* **1986,** *90* (12), 2555-2560.
38. Garcia, G.; Buonsanti, R.; Runnerstrom, E. L.; Mendelsberg, R. J.; Llordes, A.; Anders, A.; Richardson, T. J.; Milliron, D. J., Dynamically modulating the surface plasmon resonance of doped semiconductor nanocrystals. *Nano Lett.* **2011,** *11* (10), 4415-20.
39. M. J. T. Frisch, G. W. S., H. B.; Scuseria, G. E.; Robb, M. A.; Cheeseman, J. R.; Scalmani, G.; Barone, V.; Petersson, G. A.; Nakatsuji, H.; Li, X.; Caricato, M.; Marenich, A. V.; Bloino, J.; Janesko, B. G.; Gomperts, R.; Mennucci, B.; Hratchian, H. P.; Ortiz, J. V.; Izmaylov, A. F.; Sonnenberg, J. L.; Williams-Young, D.; Ding, F.; Lipparini, F.; Egidi, F.; Goings, J.; Peng, B.; Petrone, A.; Henderson, T.; Ranasinghe, D.; Zakrzewski, V. G.; Gao, J.; Rega, N.; Zheng, G.; Liang, W.; Hada, M.; Ehara, M.; Toyota, K.; Fukuda, R.; Hasegawa, J.; Ishida, M.; Nakajima, T.; Honda, Y.; Kitao, O.; Nakai, H.; Vreven, T.; Throssell, K.; Montgomery, J. A., Jr.; Peralta, J. E.; Ogliaro, F.; Bearpark, M. J.; Heyd, J. J.; Brothers, E. N.; Kudin, K. N.; Staroverov, V. N.; Keith, T. A.; Kobayashi, R.; Normand, J.; Raghavachari, K.; Rendell, A. P.; Burant, J. C.; Iyengar, S. S.; Tomasi, J.; Cossi, M.; Millam, J. M.; Klene, M.; Adamo, C.; Cammi, R.; Ochterski, J. W.; Martin, R. L.; Morokuma, K.; Farkas, O.; Foresman, J. B.; Fox, D. J., *Gaussian 16*, Revision C.01; Gaussian, Inc.: Wallingford, CT, 2016.
40. Senanayake, R. D.; Lingerfelt, D. B.; Kuda-Singappulige, G. U.; Li, X.; Aikens, C. M., Real-Time TDDFT Investigation of Optical Absorption in Gold Nanowires. *The Journal of Physical Chemistry C* **2019,** *123* (23), 14734-14745.
41. Garcia-Rodriguez, R.; Hendricks, M. P.; Cossairt, B. M.; Liu, H.; Owen, J. S., Conversion reactions of cadmium chalcogenide nanocrystal precursors. *Chem. Mater.* **2013,** *25* (8), 1233-1249.
42. Liu, D.; Lei, W.; Qin, S.; Hou, L.; Liu, Z.; Cui, Q.; Chen, Y., Large-scale synthesis of hexagonal corundum-type In 2 O 3 by ball milling with enhanced lithium storage capabilities. *Journal of materials chemistry A* **2013,** *1* (17), 5274-5278.
43. Gurlo, A.; Kroll, P.; Riedel, R., Metastability of Corundum-Type In2O3. *Chemistry–A European Journal* **2008,** *14* (11), 3306-3310.
44. Wang, T.; Radovanovic, P. V., Free electron concentration in colloidal indium tin oxide nanocrystals determined by their size and structure. *The Journal of Physical Chemistry C* **2011,** *115* (2), 406-413.
45. Kato, F.; Kittilstved, K. R., Site-specific doping of Mn2+ in a CdS-based molecular cluster. *Chem. Mater.* **2018,** *30* (14), 4720-4727.
46. Soloviev, V.; Eichhöfer, A.; Fenske, D.; Banin, U., Molecular limit of a bulk semiconductor: Size dependence of the “band gap” in CdSe cluster molecules. *Journal of the American Chemical Society* **2000,** *122* (11), 2673-2674.
47. King, P.; Veal, T. D.; Fuchs, F.; Wang, C. Y.; Payne, D.; Bourlange, A.; Zhang, H.; Bell, G. R.; Cimalla, V.; Ambacher, O., Band gap, electronic structure, and surface electron accumulation of cubic and rhombohedral In 2 O 3. *Physical Review B* **2009,** *79* (20), 205211.
48. Li, S.-S.; Xia, J.-B., Electronic structures of N quantum dot molecule. *Appl. Phys. Lett.* **2007,** *91* (9), 092119.
49. Morkoc, b. H.; Strite, S.; Gao, G.; Lin, M.; Sverdlov, B.; Burns, M., Large-band-gap SiC, III-V nitride, and II-VI ZnSe-based semiconductor device technologies. *J. Appl. Phys.* **1994,** *76* (3), 1363-1398.
50. Seo, W. S.; Jo, H. H.; Lee, K.; Park, J. T., Preparation and Optical Properties of Highly Crystalline, Colloidal, and Size-Controlled Indium Oxide Nanoparticles. *Adv. Mater.* **2003,** *15* (10), 795-797.

51. Dolai, S.; Nimmala, P. R.; Mandal, M.; Muhoberac, B. B.; Dria, K.; Dass, A.; Sardar, R., Isolation of Bright Blue Light-Emitting CdSe Nanocrystals with 6.5 kDa Core in Gram Scale: High Photoluminescence Efficiency Controlled by Surface Ligand Chemistry. *Chem. Mater.* **2014,** *26* (2), 1278-1285.
52. Yan, C.; Zharnikov, M.; Gölzhäuser, A.; Grunze, M., Preparation and characterization of self-assembled monolayers on indium tin oxide. *Langmuir* **2000,** *16* (15), 6208-6215.
53. Mryasov, O.; Freeman, A., Electronic band structure of indium tin oxide and criteria for transparent conducting behavior. *Physical Review B* **2001,** *64* (23).
54. Farvid, S. S.; Dave, N.; Wang, T.; Radovanovic, P. V., Dopant-induced manipulation of the growth and structural metastability of colloidal indium oxide nanocrystals. *The Journal of Physical Chemistry C* **2009,** *113* (36), 15928-15933.
55. Dunlop, L. A.; Kursumovic, A.; MacManus-Driscoll, J. L., Highly conducting, transparent rhombic/cubic indium tin oxide nanocomposite thin films. *Crystal growth & design* **2010,** *10* (4), 1730-1735.
56. Prewitt, C. T.; Shannon, R. D.; Rogers, D. B.; Sleight, A. W., C rare earth oxide-corundum transition and crystal chemistry of oxides having the corundum structure. *Inorg. Chem.* **1969,** *8* (9), 1985-1993.
57. Anderson, N. C.; Hendricks, M. P.; Choi, J. J.; Owen, J. S., Ligand exchange and the stoichiometry of metal chalcogenide nanocrystals: spectroscopic observation of facile metal-carboxylate displacement and binding. *Journal of the American Chemical Society* **2013,** *135* (49), 18536-18548.
58. Zhou, Y.; Wang, F.; Buhro, W. E., Large exciton energy shifts by reversible surface exchange in 2D II–VI nanocrystals. *Journal of the American Chemical Society* **2015,** *137* (48), 15198-15208.
59. Ito, D.; Yokoyama, S.; Zaikova, T.; Masuko, K.; Hutchison, J. E., Synthesis of ligand-stabilized metal oxide nanocrystals and epitaxial core/shell nanocrystals via a lower-temperature esterification process. *ACS nano* **2014,** *8* (1), 64-75.
60. Nyquist, R. A., *Interpreting infrared, Raman, and nuclear magnetic resonance spectra*. Academic Press: 2001.
61. Sardar, R.; Park, J.-W.; Shumaker-Parry, J. S., Polymer-induced synthesis of stable gold and silver nanoparticles and subsequent ligand exchange in water. *Langmuir* **2007,** *23* (23), 11883-11889.
62. Teunis, M. B.; Jana, A.; Dutta, P.; Johnson, M. A.; Mandal, M.; Muhoberac, B. B.; Sardar, R., Mesoscale growth and assembly of bright luminescent organolead halide perovskite quantum wires. *Chem. Mater.* **2016,** *28* (14), 5043-5054.
63. Chen, O.; Yang, Y.; Wang, T.; Wu, H.; Niu, C.; Yang, J.; Cao, Y. C., Surface-functionalization-dependent optical properties of II–VI semiconductor nanocrystals. *Journal of the American Chemical Society* **2011,** *133* (43), 17504-17512.
64. Liyanage, T.; Nagaraju, M.; Johnson, M.; Muhoberac, B. B.; Sardar, R., Reversible tuning of the plasmoelectric effect in noble metal nanostructures through manipulation of organic ligand energy levels. *Nano Lett.* **2019,** *20* (1), 192-200.
65. Lee, J. T.; Hati, S.; Fahey, M. M.; Zaleski, J. M.; Sardar, R., Surface-Ligand-Controlled Enhancement of Carrier Density in Plasmonic Tungsten Oxide Nanocrystals: Spectroscopic Observation of Trap-State Passivation via Multidentate Metal Phosphonate Bonding. *Chem. Mater.* **2022**.
66. Hester, R. E.; Plane, R. A., Metal-oxygen bonds in complexes: Raman spectra of trisacetylacetonato and trisoxalato complexes of aluminum, gallium, and indium. *Inorg. Chem.* **1964,** *3* (4), 513-517.
67. Nyquist, R. A.; Kagel, R. O., *Handbook of infrared and raman spectra of inorganic compounds and organic salts: infrared spectra of inorganic compounds*. Academic press: 2012; Vol. 4.

68. Son, J. S.; Wen, X. D.; Joo, J.; Chae, J.; Baek, S. i.; Park, K.; Kim, J. H.; An, K.; Yu, J. H.; Kwon, S. G., Large-scale soft colloidal template synthesis of 1.4 nm thick CdSe nanosheets. *Angew. Chem.* **2009,** *121* (37), 6993-6996.
69. Banfield, J., Thermodynamic analysis of phase stability of nanocrystalline titania. *J. Mater. Chem.* **1998,** *8* (9), 2073-2076.
70. Amara, H.; Nelayah, J.; Creuze, J.; Chmielewski, A.; Alloyeau, D.; Ricolleau, C.; Legrand, B., Is There Really a Size effect on the Surface Energy of Nanoparticles? **2021**.
71. Wolfe, R. L.; Murray, R. W., Analytical evidence for the monolayer-protected cluster Au225 [(S (CH2) 5CH3)] 75. *Anal. Chem.* **2006,** *78* (4), 1167-1173.
72. Plummer, L. K.; Crockett, B. M.; Pennel, M. L.; Jansons, A. W.; Koskela, K. M.; Hutchison, J. E., Influence of Monomer Flux and Temperature on Morphology of Indium Oxide Nanocrystals during a Continuous Growth Synthesis. *Chem. Mater.* **2019,** *31* (18), 7638-7649.
73. Xia, Y.; Xiong, Y.; Lim, B.; Skrabalak, S. E., Shape-controlled synthesis of metal nanocrystals: simple chemistry meets complex physics? *Angew. Chem. Int. Ed.* **2009,** *48* (1), 60-103.
74. Jansons, A. W.; Plummer, L. K.; Hutchison, J. E., Living Nanocrystals. *Chem. Mater.* **2017,** *29* (13), 5415-5425.
75. Watzky, M. A.; Finke, R. G., Nanocluster Size-Control and “Magic Number” Investigations. Experimental Tests of the “Living-Metal Polymer” Concept and of Mechanism-Based Size-Control Predictions Leading to the Syntheses of Iridium(0) Nanoclusters Centering about Four Sequential Magic Numbers. *Chem. Mater.* **1997,** *9* (12), 3083-3095.
76. Yang, Y.; Lee, J. T.; Liyanage, T.; Sardar, R., Flexible Polymer-Assisted Mesoscale Self-Assembly of Colloidal CsPbBr3 Perovskite Nanocrystals into Higher Order Superstructures with Strong Inter-Nanocrystal Electronic Coupling. *Journal of the American Chemical Society* **2019,** *141* (4), 1526-1536.
77. Prusty, G.; Lee, J. T.; Seifert, S.; Muhoberac, B. B.; Sardar, R., Ultrathin Plasmonic Tungsten Oxide Quantum Wells with Controllable Free Carrier Densities. *J. Am. Chem. Soc.* **2020,** *142* (13), 5938-5942.
78. Mulvaney, P., Surface Plasmon Spectroscopy of Nanosized Metal Particles. *Langmuir* **1996,** *12* (3), 788-800.
79. Schimpf, A. M.; Lounis, S. D.; Runnerstrom, E. L.; Milliron, D. J.; Gamelin, D. R., Redox chemistries and plasmon energies of photodoped In2O3 and Sn-doped In2O3 (ITO) nanocrystals. *J. Am. Chem. Soc.* **2015,** *137* (1), 518-24.
80. Gordon, T. R.; Cargnello, M.; Paik, T.; Mangolini, F.; Weber, R. T.; Fornasiero, P.; Murray, C. B., Nonaqueous synthesis of TiO2 nanocrystals using TiF4 to engineer morphology, oxygen vacancy concentration, and photocatalytic activity. *J. Am. Chem. Soc.* **2012,** *134* (15), 6751-61.

TOC Graphic

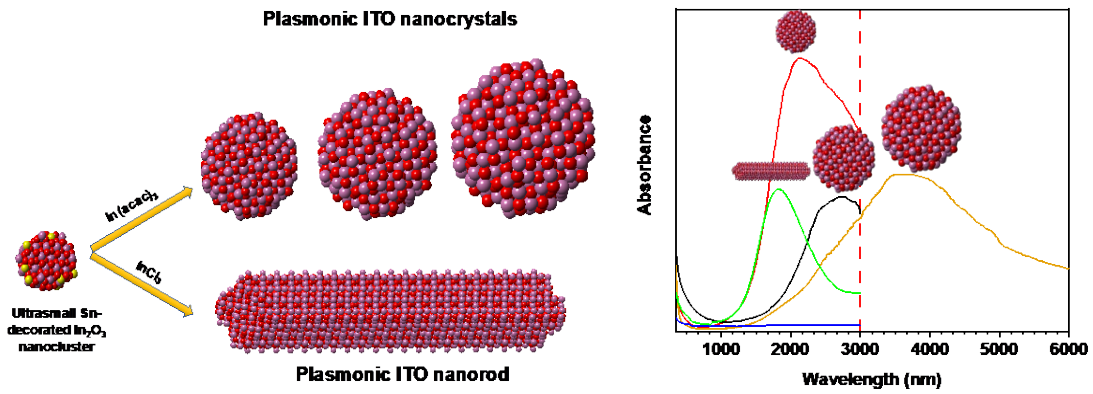
Plasmonic ITO nanocrystals
In(acac)3
InCl3
Ultrasmall Sn-decorated In2O3 nanocluster
Plasmonic ITO nanorod
Absorbance
1000
2000
3000
4000
5000
6000
Wavelength (nm)